Chapter 3

Nanofabrication and Nanocatalysis in metallogels

3.1 INTRODUCTION

In chapter 2, we synthesized a lowest possible low molecular weight symmetrical aromatic N,O donor ligand which formed yellow coloured fluorescent metallogel using LiOH in chloroform/methanol mixture. In present chapter, we again synthesized a symmetrical **H_4T^{-L-tyr}** ligand keeping the binding site similar to **H_2SA** *i.e.* N,O donor sites for metal coordination**,** to explore the effect of chirality and one extra benzene ring over the metallogel formation and its properties.

Metallogels have emerged in the last few years as an important and exciting new class of soft materials.[1,2] Inclusion of metal ions into organic gels also proved beneficial in providing additional morphological, spectroscopic, rheological, electrical,[3,28] magnetic or catalytic properties or for application in gas/dye adsorption, crystal growth and guest encapsulation.[1-5] Over the last decade, metallogels have also proved useful as active material in catalytic reactions.[9-11] There have indeed been an increased focus on hybrid materials containing catalytically-active NPs *e.g.* gold Nanoparticles (AuNps), owing to their various important interdisciplinary applications.[12] In general, AuNPs were grown using some supported media[13-14] whereas since the last decade, organic gels were being utilised as a platform for controlled growth of AuNPs.[15,16] Even after using organic gels as a platform, gold nanoparticles with diameter less than 5 nm is hardly achieved so far which is the essential criteria to accomplish good catalytic activity.[17,18] There are only few reports available where the fine sized AuNps (≤5nm) have been achieved either with supported or organic gel mediated, but achieving uniformity in size is still a challenging task.[17,18]

Catalytic activity using Nps are often studied for a model reduction reaction of 4-NP to 4-AP in presence of mild reducing agent $NaBH_4$ due to easy monitoring through UV-vis

study.[19-21] The reported rate constants for first order kinetics for such model reaction usually lies in the range of 0.05 min^{-1} to 2.5 min^{-1} values.[19-21] Exceptionally high values of rate constants were usually achieved from the AuNPs synthesized over support media or using external stabilizing agents such as; SiO_2 yolk/shell,[19] CTAB[20] and polyethylene glycol[21] *etc*. A large number of reports are available for synthesis of AuNps within the organo-organic-gels matrix, but none of them utilized for aforementioned reduction reaction.[22] In particular, AuNPs containing hydrogels (Au-HYs) utilized for model reduction reaction were usually synthesized from polymeric materials and the rate constant were reported between 0.09 to 0.45 min^{-1}.[23,24] Only a few metallogel media are utilized for controlled growth of nanoparticles using nanofibers as platform.[6-8] Steed and Jung *et al*. have disjointedly reported some early examples of such achievements, with the *in situ* growth of Ag nanoparticles in metallogel matrix used as nanocatalyst in reduction reactions.[6,7] Also, a series of *tris* (pyridylamide)-based metallogels have recently been used as a media for studying the growth and the catalytic properties of silver nanoparticles in the reduction of *p*-nitrophenolate to *p*-aminophenolate.[8] None of the reports deduced the kinetic parameters (k_{app}, E_a, $\Delta S^{\#}$ and $\Delta H^{\#}$) of reduction reaction. The size/surface area of nanoparticles is a key parameter in nanocatalysis and a number of previous reports have revealed that the fibres present in metallogels can be used as templates to control the growth of NPs.[6-8] Thus, the uniform size of AuNPS in gel matrix with good catalytic behavior is comparatively less achieved.

In general, conductive soft materials are of utmost importance for energy conversion and storage purposes. They find useful applications in batteries, fuel cells, electrochemical supercapacitors, solar cell and electronic skin.[25-27] In that regard, the conductance as an

inherent property of metallogels has recently become a subject of increasing attention.[3,28] Most of the conductive gels reported so far exhibit conductivity values ranging from 10^{-4} to 10^{-2} S cm^{-1}.[29-32] Moreover, the high conductivity measured in the gel states usually involve conventional polymers[29]/molecules[30,31] or doping with suitable additives[32]. Some gels have also been shown to behave as protons conductors with conductivity values falling in the range of $2.4x10^{-2}$ to $1.4\ x10^{-4}$ S cm^{-1} in the xerogel state.[28] In line with these issues, we have recently reported the ultrasound-induced formation of metallogels coming along with an unprecedented ~10 fold enhancement in the conductivity values going from 0.45 to $4.06\ x10^{-4}$ S cm^{-1}.[3] However, the design and synthesis of highly conductive metallogels still remains a challenging task.[33]

Besides, none of the studies reported so far involve coordination polymers metallohydrogels displaying simultaneously catalytic and conductance properties.

In line with the above mentioned issues and challenges, this chapter focuses towards the synthesis and properties of fluorescent coordination polymer metallohydrogels (**CPH**) obtained from sequential mixing of LiOH and $Zn(NO_3)_2$ to a L-tyrosine derived low molecular weight pro-ligand $H_4T^{-L\text{-}tyr}$ (scheme 3.1).[34,35] Further, our study also includes the nanofabrication of Au nanoparticles used as active sites in the catalytic reduction of *p*-nitrophenol and conductance measurements carried out on gels samples.

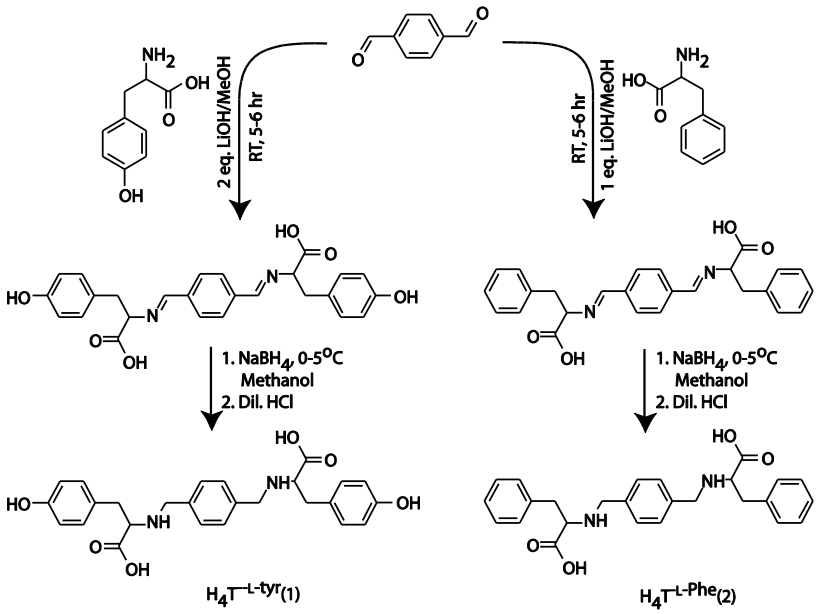

Scheme 3.1 Synthetic route adopted for the synthesis of $H_4T^{\text{-L-tyr}}$ and $H_4T^{\text{-L-Phe}}$.

3.2 EXPERIMENTAL METHODS

3.2.1 Materials and physical methods

Reagents and solvents used in experiment were purchased from Sigma-Aldrich Chemicals Pvt. Ltd., Spectrochem Pvt. Ltd., and S. D. Chem-Limited. The solvents were distilled before using in synthesis by following standard methods. Terephthaldehyde and D_2O were purchased from Sigma-Aldrich. L-Tyrosine and L-Phenylalanine were purchased from S. D. Chem-Limited and Spectrochem Pvt. Ltd., respectivley.

FTIR and UV-Vis study of pro-ligands were done on PerkinElmer- spectrum 100 FTIR and Thermo scientific evolution 200 spectrophotometer, respectively. Photoluminescence spectra were acquired on a Perkin Elmer LS 55 spectrophotometer. ^{1}H NMR spectra were obtained on a Bruker AVANCE III HD 500 spectrometer. Electrospray ionization mass (ESI-MS) spectra were recorded on a Waters (Micromass MS Technologies) QTof Premier. Thermal Gravimetric analysis data was acquired on a NETZSCH TG209 F1 Libra

TGA209FlD-0105-l at a heating rate of 5 °C min^{-1} under a nitrogen atmosphere. TEM images were captured using a JEOL JEM 2100. Powder XRD data was collected on Rigaku SmartLab between angle 2θ = 5–80°. Rheology of metallohydrogel was performed on Anton Paar Quality Control Rheometer RheolabQC.

Impedance measurements have been carried out with a Biologic® ESP 300 potentiostat equipped with a built-in computer-controlled Frequency Response Analyzer **(**FRA) operating over a frequency range of 10 μHz up to 7 MHZ. Home-made one-compartment, two-electrode cells allowing to position two identical cofacially oriented stainless steel or platinum electrodes at a fixed distance has been used to estimate the conductivity of each sample. Variable temperature measurement of the conductivity have been carried out in a home-made jacketed glass cell incorporating two platinum electrodes (Ø = 1cm). The temperature in the cell was controlled with a Lauda-Brinkman RE 104 thermostat. Electrical impedance measurements have been performed in a potentiostatic regime at E_{oc} between 1Hz and 2.5MHz using a maximum voltage of 0.01V. Fitting the experimental Nyquist impedance diagrams (–Im(Z) *vs.* Re(Z)) was achieved with Z-fit using equivalent electrical circuits involving the actual resistance of the sample R_1, a capacitance C_1 and a constant-phase element Q_1. Such fitting allowed to estimate the resistance of each samples corresponding to the intersection of the curve with the real part of the impedance. The conductivity was calculated from the electrolyte resistance (R_1) using the equation:

$$\sigma = l / R_1 \kappa$$

Where κ is the conductivity in $S.m^{-1}$, R is the ohmic resistance of the electrolyte, l is the distance between the two electrodes (m) and S is the area of the electrodes (m^2). The cell constant, (l/S) was determined at 25°C by calibration with *standard* 0.001D, 0.01D and 0.1D

KCl *solutions* having known *conductivity* values, (1408 $\mu S.m^{-1}$, 1285 $mS.m^{-1}$ and 11.13 $S.m^{-1}$).

3.2.1.1 Rheological Study

The rheological measurements were performed on freshly prepared metallohydrogel with (**AuCPH**) and without AuNps (**CPH**) in triplicate. The measurements were carried out using a stress-controlled rheometer model *Anton Paar Quality Control Rheometer RheolabQC* instrument equipped with stainless steel parallel plates (20 mm diameter, 0.2 mm gap). Experiments were performed on freshly prepared metallohydrogel (1 % w/v). Linear viscoelastic regions of the metallogel samples were determined by measuring the storage modulus, G′ (associated with energy storage) and the loss modulus, G″ (associated with the loss of energy) as a function of stress amplitude (Dynamic oscillatory frequency of 10 rad s^{-1}). The following tests were performed: increasing amplitude of oscillation up to 100 % apparent strain on shear, time and frequency sweeps at 25 °C (20 min and range from 0.05 to 100 rad s^{-1}, respectively) and a heating run to 100 °C at a scan rate of 5 °C min^{-1}.

3.2.2 Synthetic procedure

3.2.2.1 Synthesis of $H_4T^{-L\text{-}tyr}$

It was synthesized by following the standard literature with some modification.[46] L-tyrosine (0.200 g, 1.1 mmol) and $LiOH{\cdot}H_2O$ (0.069 g, 1.64 mmol) were dissolved in dry methanol (15 mL) and stirred for 15 min at room temperature. Methanolic solution of terephthaldehyde (0.185 g, 1.37 mmol) was added to the above solution and stirred for an additional 5 hours. Resulting mixture was reduced with sodium borohydride (0.168 g, 4.412 mmol). Upon neutralisation with dilute HCl, it afforded a white solid, thoroughly washed with water, diethylether and dried under vaccuum. Yield 0.440 g (85%). Anal. Calc. for

$C_{26}H_{28}N_2O_6$: C, 67.21; H, 6.07; N, 6.03. Found C, 68.02; H, 6.83; N, 5.79. Due to poor solubility of the neutral form, ^{1}H NMR, ^{13}C NMR and UV-vis measurements were performed by dissolving the solid in D_2O in presence of 3 equiv. of $LiOH{\cdot}H_2O$. ^{1}H NMR (500 MHz, D_2O, ppm): δ 7.27 (s, 4H, Ar), 6.95 (d, 4H, Ph), 6.54 (d, 4H, Ph), 3.72 (d, 2H, $-CH_2Ph$), 3.54 (d, 2H, $-CH_2Ph$), 3.28 (t, 2H, $-CHNH$), 2.75 (m, 4H, $-CH_2NH$). ^{13}C NMR (400 MHz, D_2O, ppm): δ 179.81, 158.35, 141.52, 130.23, 129.10, 128.72, 120.25, 65.92, 51.82, 31.60. FTIR (KBr, cm^{-1}) ν_{as}(COO) 1615(s). UV-vis spectrum (water): (λ_{max}, nm; ε, $M^{-1}cm^{-1}$) 275 (2800), 222 (sh).

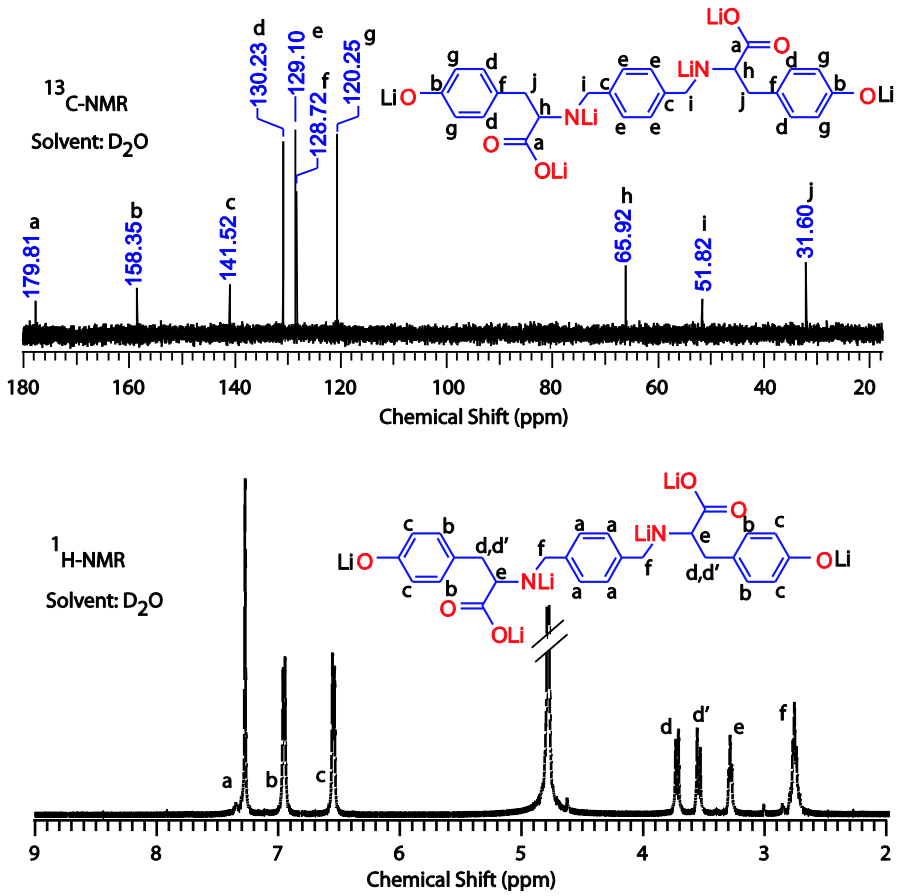

Figure 3.1 ^{13}C (above) and ^{1}H NMR (below) spectrum of LiOH deprotonated $H_4T^{\text{-L-tyr}}$ (D_2O). Chemical structure of $H_4T^{\text{-L-tyr}}$ along with alphabetic assignment of carbons and protons, respectively, and its corresponding peak is shown in spectrum.

3.2.2.2 Synthesis of $H_4T^{-L\text{-}Phe}$. It was synthesized following the above procedure for $H_4T^{-L\text{-}tyr}$ using L-phenylalanine instead of L-tyrosine. Yield 0.480 g (92%). Anal. *calcd* for $C_{26}H_{28}N_2O_4$: C, 72.20; H, 6.53; N, 6.48. Found C, 72.88; H, 7.02; N, 6.37. Due to poor solubility of the neutral form, ^{1}H NMR and UV-vis measurements were performed by dissolving the solid in D_2O in presence of 2 equiv. of $LiOH{\cdot}H_2O$. ^{1}H NMR (D_2O, 500 MHz, ppm): δ 7.35-7.21 (m, 14H, Ar & Ph), 3.72 (d, 2H, $-CH_2Ph$), 3.54 (d, 2H, $-CH_2Ph$), 3.34 (t, 2H, $-CHNH$), 2.89 (m, 4H, $-CH_2NH$). ^{13}C NMR (400 MHz, *d*$_6$-DMSO, ppm): δ 177.74, 141.50, 139.67, 129.93, 128.13, 125.8, 127.86, 65.31, 52.21, 31.20. FTIR (KBr, cm^{-1}) ν_{as}(COO) 1570(s). UV-vis spectrum (water): (λ_{max}, nm; ε, $M^{-1}cm^{-1}$) 260 (1200).

3.2.2.3 Synthesis of gold nanoparticle embedded metallohydrogel (AuCPH). Synthesis of **AuCPH** involved, as a last step prior to gelification of **CPH**, the slow addition of a given volume (V_{AuNP}) of a freshly prepared $HAuCl_4$ solution ($HAuCl_4$, 10^{-1} $molL^{-1}$ in methanol/diethylether, 100 µL-400 µL) to a mixture of ligand/ $LiOH/Zn^{2+}$ salt. An instant and drastic change in colour of **CPH** from white to red was obtained without disturbance in

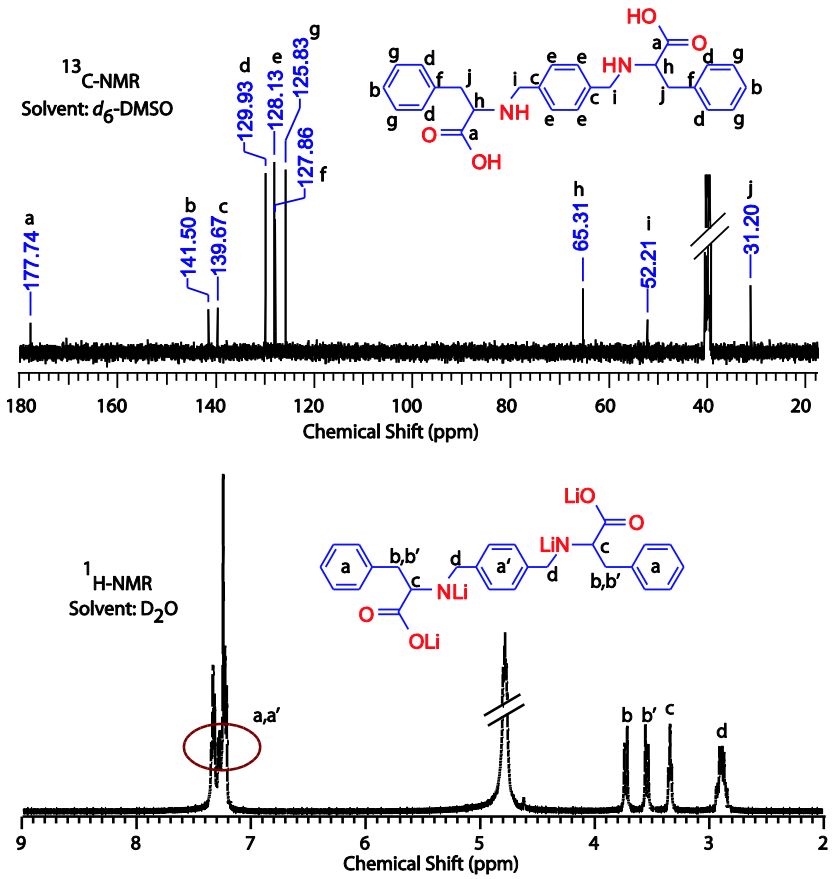

Figure 3.2 ^{13}C (above) spectrum of $\mathbf{H_4T^{\text{-L-Phe}}}$ in d_6-DMSO and ^{1}H NMR (below) spectrum of LiOH deprotonated $\mathbf{H_4T^{\text{-L-Phe}}}$ (D_2O). Chemical structure of $\mathbf{H_4T^{\text{-L-Phe}}}$ along with alphabetic assignment of carbons and protons, respectively, and its corresponding peak is shown in spectrum.

appearance of **CPH**. The **AuCPH** was further subjected to characterization with suitable instrumental techniques like FTIR (KBr, cm^{-1}): ν_{as}(COO) 1615(s). UV-vis spectrum (water): (λ_{max}, nm; ε, $M^{-1}cm^{-1}$) 275 (2400), 560 (br). TEM: diameter of nanoparticle ~3 nm.

3.2.2.4 TEM sample preparation. Samples for TEM analysis was prepared by diluting 1 mL of gel in a 15 mL water. 1 to 3 drops of this solution were placed on a carbon-coated copper grid (400 mesh) and dried in dust free vacuum for 2 days. After complete drying, the specimens were examined with a JEOL JEM-2100 transmission electron microscope

operating at 200 kV using an accelerating voltage of 100 kV and a 16 mm working distance.

3.3 RESULTS AND DISCUSSION

The chiral low molecular weight pro-ligands $H_4T^{\text{-L-tyr}}$ and $H_4T^{\text{-L-Phe}}$ have been obtained in good yields from L-Tyrosine and L-Phenylalanine amino acids, respectively (Scheme 3.1). We found that transparent metallohydrogel (**CPH,** 1% w/v) readily forms at pH 11-12 and ambient temperature after deprotonation of $H_4T^{\text{-L-tyr}}$ with an aqueous solution of $LiOH{\cdot}H_2O$ followed by gradual addition of $Zn(NO_3)_2{\cdot}6H_2O$ in a 1:3:1 ratio (section 3.2.2). The gel was preliminary tested by standard methods like the 'inverted vial' and 'falling ball" tests (Figure 3.3 and 3.33). The key role of alkali ions in the gelation process was revealed upon substituting Li^+ for Na^+, K^+ or Cs^+ and finding out that such replacements result in a significant increase of the gelation time and in a decrease of the gel strength, which might be due to the high hydration capability of Li^+ compared to the other alkali metal ions.[3,43-46] It is also further supported by the fact that non-alkali bases like, TBAOH, NH_3 or Et_3N failed to produce gels (Figure 3.3 and 3.4).

Solvent	**$H_4T^{\text{-L-tyr}}$ +LiOH+$Zn(NO_3)_2$**	**$H_4T^{\text{-L-Phe}}$ +LiOH+$Zn(NO_3)_2$**
Water	**Gel**	Gelatinous Solution
Acetonitrile	Solution	Solution
MeOH	Solution	Solution
Ethanol	Solution	Solution
DMSO	Solution	Solution

Table 3.1 Gelation details isomer, cation and solvent

Solvent	**LiOH**	**NaOH**	**KOH**	**CsOH**
Water	**Gel**	Weak Gel	Weak Gel	Gelatinous Sol

Table 3.2 Gel or sol formation of **$H_4T^{\text{-L-tyr}}$** with different alkali bases and $Zn(NO_3)_2$

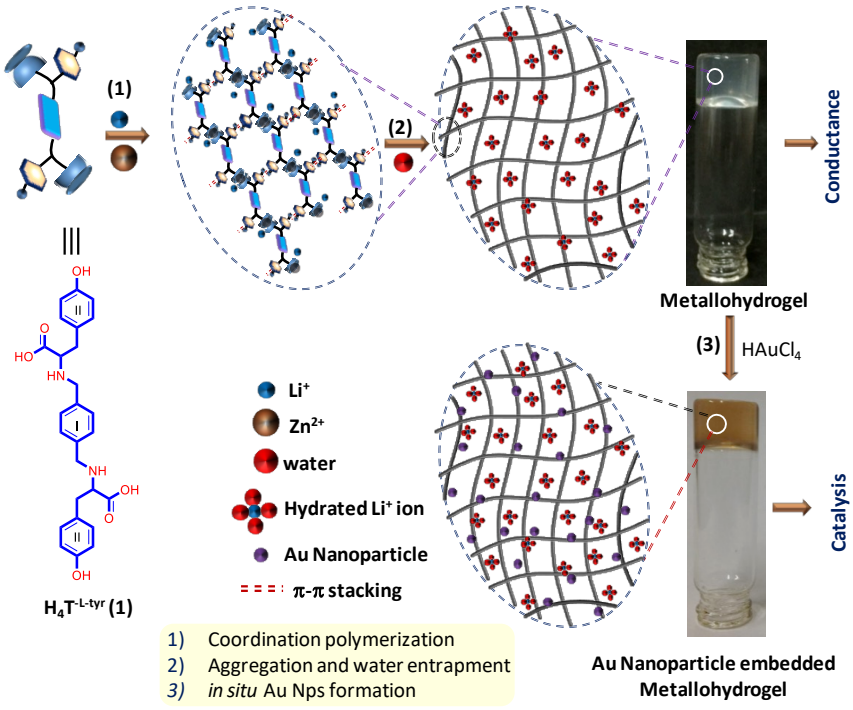

Figure 3.3 Pictorial presentation of mechanism involved in metallohydrogel (**CPH**) and AuNps embedded metallohydrogel (**AuCPH**) formation.

Formation of **CPH** was also found to require the presence of water as a solvent and of $Zn(NO_3)_2$ as an assembling element. The importance of both the cation and the anion species was brought to light with all our attempts to replace either Zn^{2+} or NO_3^- ions failing to produce gels (Table 3.1). Then, use of pro-ligand $H_4T^{\text{-L-Phe}}$ (Scheme 3.1) instead of $H_4T^{\text{-L-tyr}}$ only led to the formation of gelatinous solutions, which suggests the implication of the –OH groups in the gelation process (Figure 3.4). The synthesis of **CPH** was thus found to exhibit a multi-dimensional selectivity towards ligand, base, $Zn(NO_3)_2$, solvent and pH. The freshly synthesized **CPH** was transparent enough to read a text through it and was found to emit blue light when exposed to UV irradiation of λ= 365 nm (Figure 3.5). Gel-sol phase transitions could also be reversibly triggered using external stimuli such as temperature, ultrasound and mechanical force (Figure 3.6). CPH also has shape persistence and reswelling behavior

(Figure 3.6). Remarkably, the **CPH** can be stored at 20 °C for more than a year without change in appearance or transparency.

We also discovered that dark pink gold nanoparticles (NPs) can be grown inside **CPH** matrix in the absence of reducing agent by simple addition of a methanolic/ether solution of $HAuCl_4$ (Figure 3.3). Formation of AuNPs was unambiguously demonstrated by the observation of a diagnostic surface Plasmon resonance (SPR) signal centered at *ca.* 560 nm (Figure 3.7).[36]

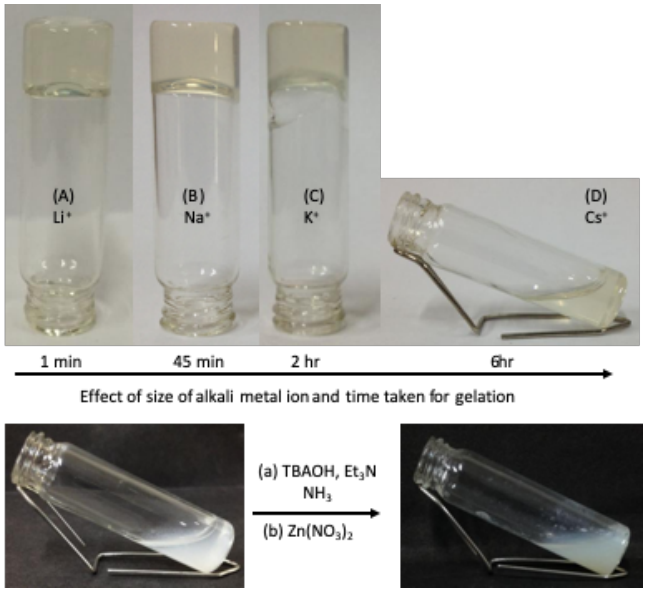

Figure 3.4 (A) Monitoring of gel strength and effect of size of alkali metal ions Li^+, Na^+, K^+ and Cs^+. Moving from Li^+ to Cs^+ gelation time increases and weakens the strength of gel. (B) Gelatinous solution obtained when we replace $H_4T^{-L\text{-}tyr}$ with $H_4T^{-L\text{-}Phe}$ under similar gel synthesis conditions, (C) and (D) Gelation test with other bases like TBAOH or Et_3N or NH_3 produce turbid solutions.

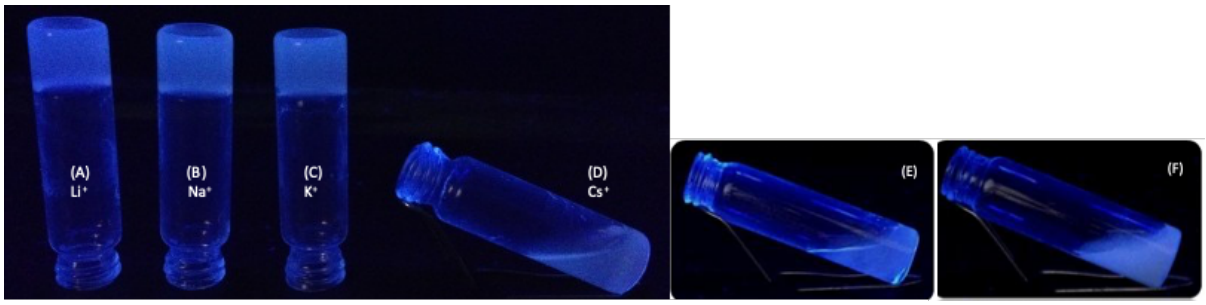

Figure 3.5 (A) Metallogel/solution under UV lamp (λ_{em}=365 nm), (B) $H_4T^{-L\text{-}Phe}$ produced fluorescent gelatinous solution under similar conditions and (C) TBAOH deprotonated $H_4T^{-L\text{-}tyr}$ produced fluorescent precipitate under similar condition to gelation.

As for the formation mechanism, the reduction of Au(III) to Au(0) and the subsequent deposition of the nanoparticles over the nanofibers, although not fully understood, might potentially be achieved through the oxidation of the electron donating amine (-NH) functions available in $H_4T^{-L\text{-}tyr}$.[6,37] A detailed characterization of the **CPH** and **AuCPH** materials is provided in the following sections. It also includes catalytic studies, where freshly prepared AuNP-doped **CPH** proved useful to achieve the reduction of *p*-nitrophenol into the corresponding amino-phenol (Figure 3.27).

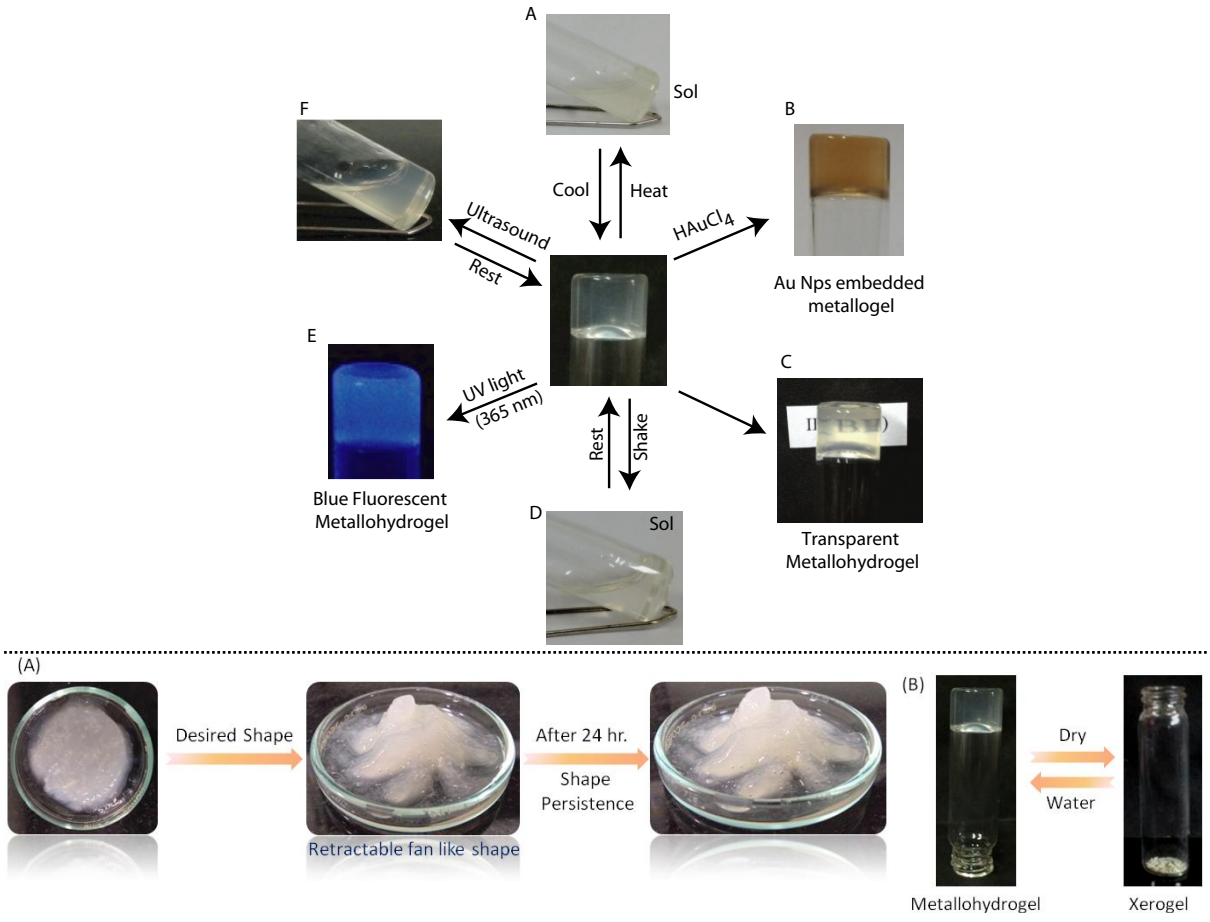

Figure 3.6 (Upper) Various properties of metallohydrogel- (A), (D) and (F) shows the multi-stimuli responsive behavior of metallohydrogel towards external stimuli temperature, mechanical and ultrasound, (B) Au nanoparticle containing metallohydrogel (**AuCPH**), (C) The freshly prepared transparent metallogel, through which word is readable, (E) Blue fluorescent metallohydrogel under UV lamp (365 nm). (Lower) (A) Shape persistence

property of metallohydrogel which was retained even after 24 hrs and (B) Reswelling behavior shown by metallohydrogel (**CPH**). (Thermoreversibility was monitored at 70°C.)

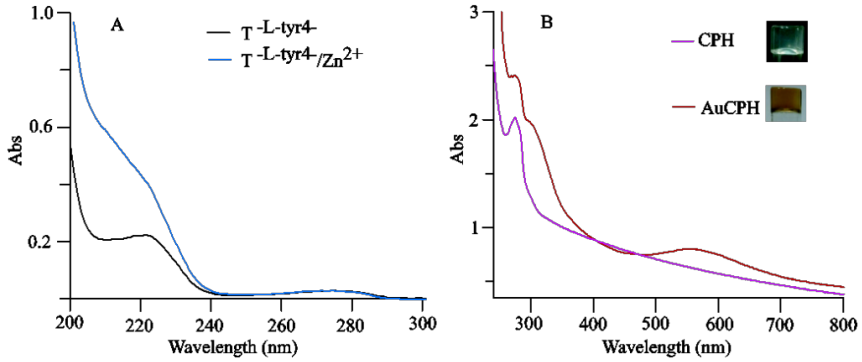

Figure 3.7 UV-vis spectra of **(A)** $T^{-L\text{-}tyr4-}$ ($1X10^{-5}$M, H_2O, black line) and upon addition of $Zn(NO_3)_2$ in blue line and (B) A comparsion spectra of diluted AuCPH (red line) and **CPH** (voilet line).

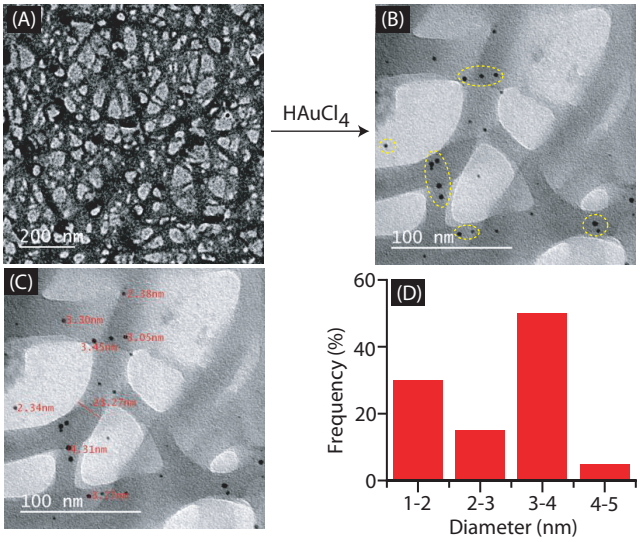

Figure 3.8 TEM images of **(A)** metallogel **CPH**, **(B) AuCPH** shows the AuNPs fabricated onto the fibers, **(C)** size distribution of AuNPs and **(D)** size distribution histogram for AuNPs.

3.3.1 Morphological characterization

Transmission electron microscopy (TEM) measurements provided key insight into the morphology of **CPH** and **AuCPH** (Figure 3.8-3.10). Images recorded with Transmission electron microscopy (TEM) measurements provided key insight into the morphology of **CPH**, **AuCPH** and size distribution of AuNPs. Images recorded with **CPH** revealed a uniform and long-range branched nano-fibrous morphology, with an average fiber diameter

of ~20 nm. In **AuCPH**, the observation of average nanometer-size AuNPs (~3nm), with an apparent narrow size distribution, uniformly deposited over the fibers suggests the key role of the chemical functions available at the surface of the fibers in directing the reduction-induced growth of the NPs. The uniform spatial distribution of AuNPs was further supported through FE-SEM elemental maps for Au in xerogel of **AuCPH** (Figure 3.11). Dynamic Light Scattering (DLS) analyses conducted on **AuCPH** (**4**) unfortunately failed to provide the exact size distribution of the AuNPs, most probably due to presence of nanofibers inside the gel matrix.

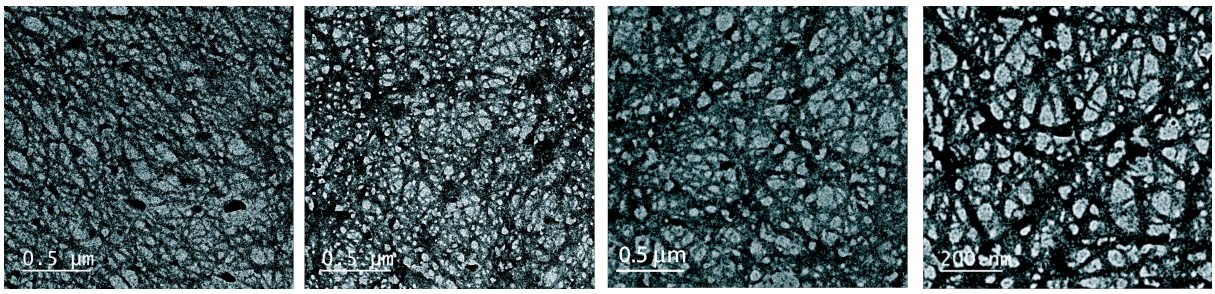

Figure 3.9 TEM images of diluted **CPH** ($1X10^{-5}$M) at two different magnification.

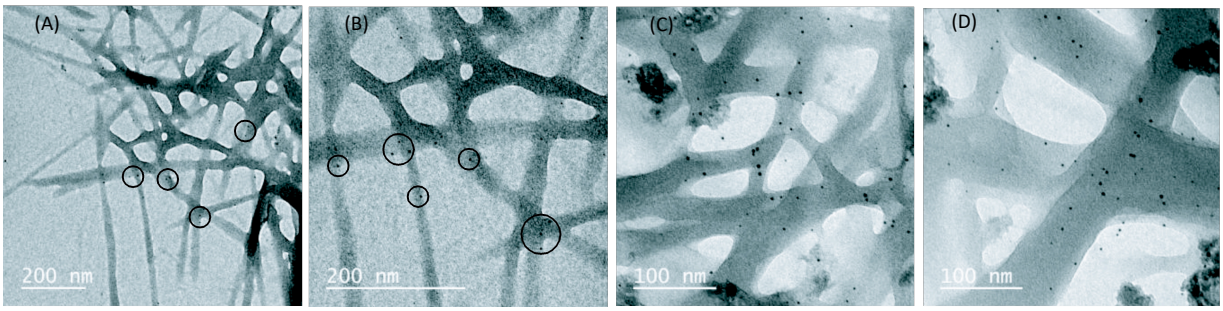

Figure 3.10 TEM images of diluted **AuCPH** captured at three different magnifications.

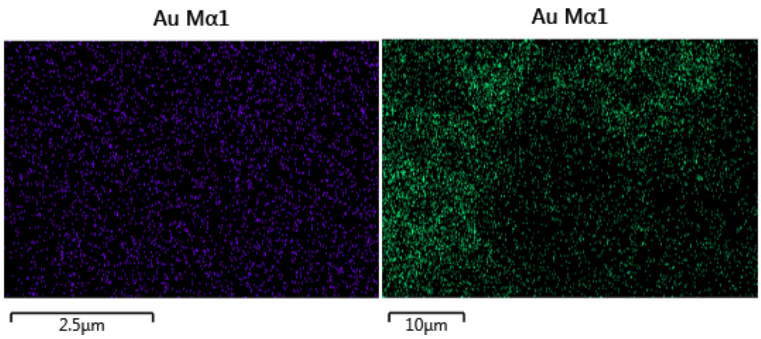

Figure 3.11 FE-SEM elemental maps for AuNps dispersion in xerogel state performed

twice to ensure the homogeneous dispersion. The colors in the element map are violet (left) and green (right) for AuNPs.

X-ray powder diffraction (PXRD) experiments have been carried out with the metal free pro-ligand $H_4T^{-L\text{-}tyr}$ and with dried **CPH** samples (xerogel) to gain further insight into the arrangement and packing pattern of the nanofibers. The PXRD patterns collected with $H_4T^{-L\text{-}tyr}$, display intense crystalline peaks at $2\theta = 8^o$, 17^o, 20^o, 21.5^o, 26^o (Figure 3.12). The pattern recorded with xerogel obtained from CPH includes a broad diffraction peak centered at 20° accounting for the amorphous nature of the dried gel[38] and an intense peak at 21.22° consistent with the presence of stacking pattern in **CPH** with a *d*-spacing value of 4.18 Å.[39] Then, the reflection observed at 3.82 Å ($2\theta = 23.24^o$) is attributed to a regular stacking (π–π) of the individual ligands in the fibers.[40] The pattern also includes a series of peaks (*d*-spacing ranging from 2.3-2.83 Å) assigned to hydrogen bonding interactions involved in the formation of fibers and in the gelification.[57,58]

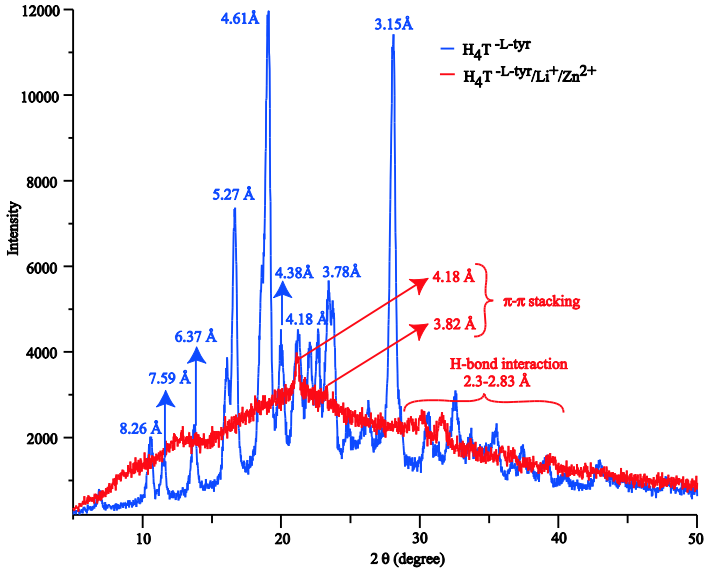

Figure 3.12 Powder X-Ray Diffraction pattern of $\mathbf{H_4T^{-L\text{-}tyr}}$ (blue line) and xerogel (Red line).

3.3.2 Aggregation studies

Fluorescence measurements have been carried out to further characterize the chemical processes involved in the formation of **CPH**. The fluorescence spectra of LiOH deprotonated $\mathbf{H_4T^{-L\text{-}tyr}}$ ($1x10^{-2}$ M, H_2O, λ_{ex}= 275 nm) showed two peaks centered at 330 nm (Stokes shift= 6000 cm^{-1}) and 408 nm (Stokes shift= 11800 cm^{-1}) attributed to π–π* and n-π* transitions, respectively. Addition of increasing amounts of $Zn(NO_3)_2$ (1M solution in H_2O) led to a blue shift of about 7 nm of both emission signals coming along with a significant enhancement (~+90%) in intensity (Figure 3.13). The latter effect is attributed to a reduction of the non-radiative decay through a rigidification of the ligand backbone upon chelation with Zn^{2+}.[41] The fact that the emission intensity at 330 nm, associated to π–π* transitions, increases to a much larger extent than that recorded at 408 nm also suggest that π–π stacking interactions are involved in the aggregation process leading to gelation (Figure 3.13).

Similar investigations carried out on non-gelling combinations of ligand/base/metal, *viz*: $\mathbf{H_4T^{-L\text{-}tyr}}/Cs^+/Zn^{2+}$, $\mathbf{H_4T^{-L\text{-}tyr}}$/TBAOH/$Zn^{2+}$, $\mathbf{H_4T^{-L\text{-}tyr}}/Li^+/Zn(OAc)_2$ and $\mathbf{H_4T^{-L\text{-}tyr}}/Li^+/Cu^{2+}$, served to confirm the selectivity of the gelation process towards each components (Figure 3.14-3.16). The importance of lithium ions in the gelification of $\mathbf{H_4T^{-L\text{-}tyr}}/Li^+/Zn(NO_3)_2$ mixtures was revealed upon showing that the substitution of Li^+ with any other alkali ion yielded either weak gels or clear ungelified solutions coming along with a decrease in the intensity of both emission signals (Figure 3.33 and Figure 3.14). Then, addition of Zn^{2+} to $\mathbf{H_4T^{-L\text{-}Phe}}$ in the same conditions as above was found to result in a much lower increase (~+40%) of the emission signals centered at 328 nm (Stokes shift= 8300 cm^{-1}) and 396 nm (Stokes shift= 13500 cm^{-1}). Formation of zinc

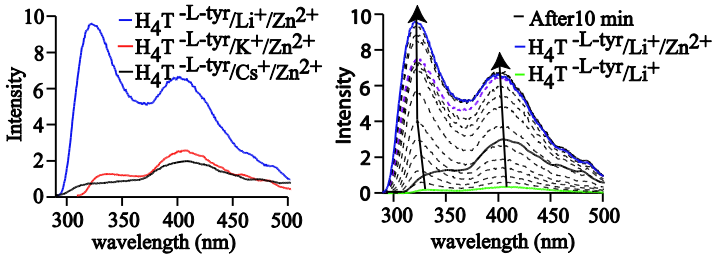

Figure 3.13 (A) A fluorescence spectra of $\mathbf{H_4T^{-L\text{-}tyr}}$ with Li^+/Zn^{2+} (blue line), K^+/Zn^{2+} (red line) and Cs^+/Zn^{2+} (black line) in water, **(B)** Titration between $\mathbf{H_4T^{-L\text{-}tyr}}$, $/Li^+$ *vs* Zn^{2+} [$\mathbf{H_4T^{-L\text{-}tyr}}$, λ_{ex}= 275 nm, $1x10^{-2}$ M, H_2O; LiOH, 3 M, H_2O; $Zn(NO_3)_2$, 1M, H_2O].

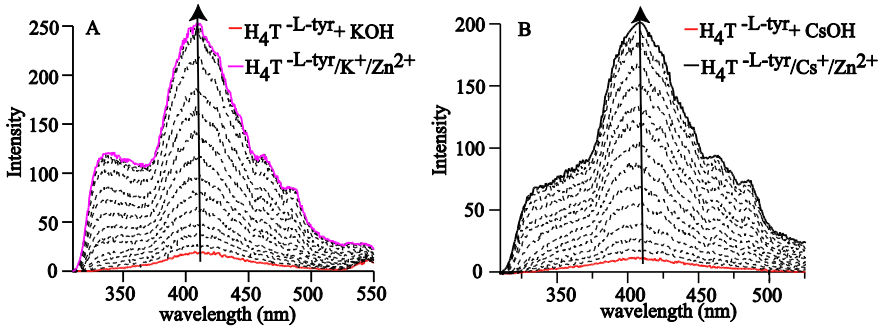

Figure 3.14 Fluorescence titration of (A) KOH deprotonated $T^{-L\text{-}tyr4-}$ ($1x10^{-2}$M, H_2O, λ_{ex}= 275 nm) with $Zn(NO_3)_2$ shows the gradual enhancement in intensity of the peak at 411 nm (stoke's shift= 12000 cm^{-1}) and a new peak generation at 338 nm with no noticeable shift and (B) CsOH deprotonated $T^{-L\text{-}tyr4-}$ ($1x10^{-2}$M, H_2O, λ_{ex}= 275 nm) produced the same fluorescence spectra.

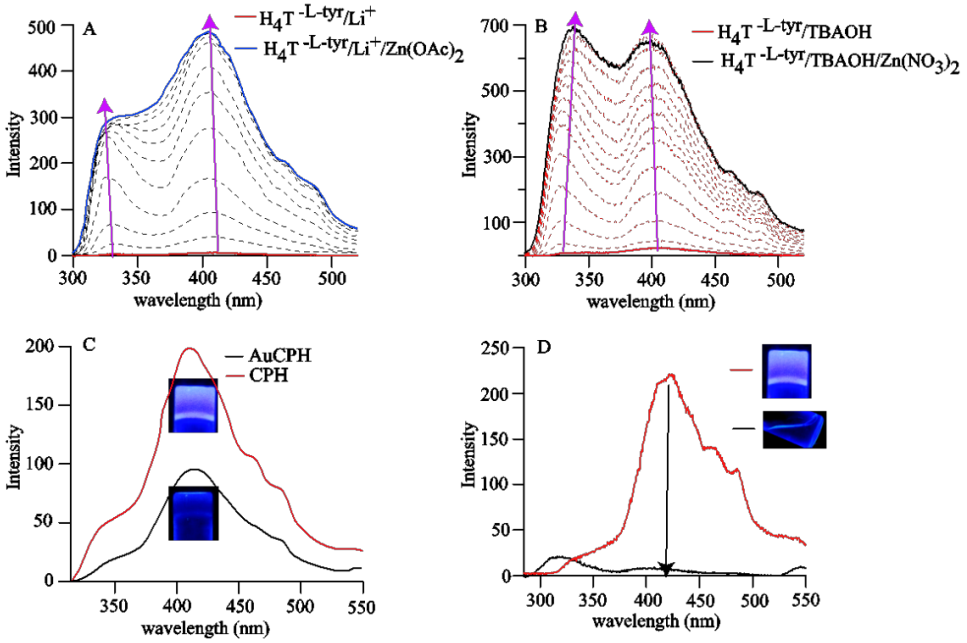

Figure 3.15 Fluorescence experiment **(A)** LiOH deprotonated $T^{-L\text{-}tyr4-}$ (red line) appears 330 nm and 408 nm which upon gradual addition of 1.2 equivalent of $Zn(OAc)_2$ (blue line) increases the emmision intensity, **(B)** Fluorescence spectra of TBAOH deprotonated

$T^{-L\text{-}tyr4-}$ (10^{-2}M, H_2O) with $Zn(NO_3)_2$ shows enhancement in instensity with smalll red shift of 8 nm at 330 nm peak and small blue shift of 6 nm of 406 nm peak, **(C)** A comparative fluorescence spectra of CPH and AuCPH and **(D)** Fluorecence spectra of CPH upon treatment with HCl.

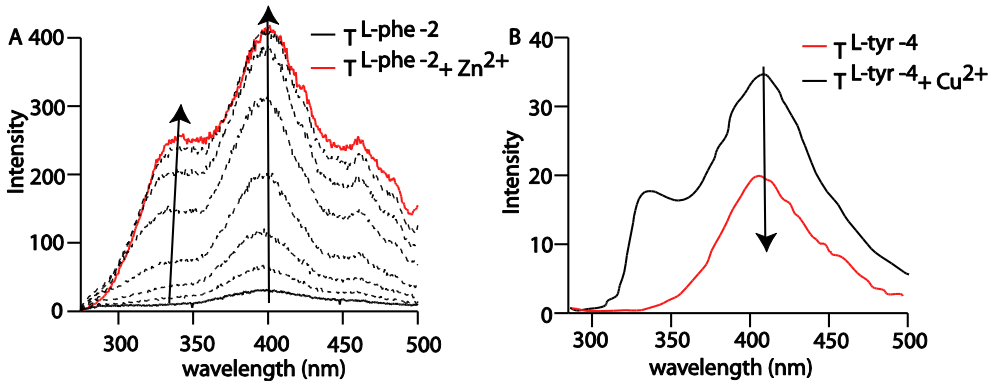

Figure 3.16 (A) Fluorescence spectra of LiOH deprotonated $H_4T^{-L\text{-}Phe}$ (10^{-2}M, H_2O, λ_{ex}= 258 nm) with $Zn(NO_3)_2$ (1M, H_2O) and (**B**) Addition of $Cu(NO_3)_2$ to $T^{-L\text{-}tyr4-}$ (10^{-2}M, H_2O, LiOH deprotonated) produced nonfluorescent complex.

adducts with $\mathbf{H_4T^{-L\text{-}Phe}}$ also led to a red shift of about 11 nm of the emission band at higher energy (π–π*), to be compared to the 7 nm blue shift observed in the same conditions with $\mathbf{H_4T^{-L\text{-}tyr}}$, which is in agreement with the formation of two disctint molecular arrangement (Figure 3.13, 3.16 and 3.19).

The aggregation process involved in the formation of **CPH** was further demonstrated upon carrying out fluorescence measurements (λ_{ex}= 275 nm) on gel samples obtained at different concentrations. The curves collected in Figure 3.17 have been recorded after multiple dilutions of a freshly prepared **CPH** gel, from 10^{-2} M (red line) down to $5X10^{-4}$ M (black line). These data reveal that dilution results in a large increase in the emission intensity at 338 nm (π–π*) associated to a continuous blue shift of the maximum emission wavelength (reaching 22 nm at $0.5X10^{-3}$ M), the latter changes being observed while the emission peak at 411 nm (n-π*) remained unchanged throughout the dilution experiment. The emission at 338 nm was found to reach a maximum value at about $0.5X10^{-3}$ M and then

to go down with further dilution losing about 90% of its initial intensity at $1X10^{-4}$ M. This drastic drop in intensity is here also associated to a continuous blue shift of the max wavelength going from 311 to 307 nm when concentration is decreased from $0.5X10^{-3}$ M to $1X10^{-4}$ M. The successive increase and decrease of the emission intensity observed upon dilution of the gel can be attributed to a combination of segregation and dilution effects. The increase in intensity observed with increasing dilution, *i.e.* from $1X10^{-2}$ aggregation caused quenching (ACQ) phenomena promoted by the gelification process.[42] Then the intensity drop observed at the lower end of the concentration range ($0.5X10^{-3}$ to $1X10^{-4}$ M) is attributed to a simple dilution of the fluorescent entities. The overall blue shift of about 31 nm observed over the entire dilution range is most probably related to changes in the π–π stacking modes. Thus, at this stage, we assume that the π–π stacking might be responsible for aggregation followed by gelification, which is consistent with the results obtained from PXRD experiments.

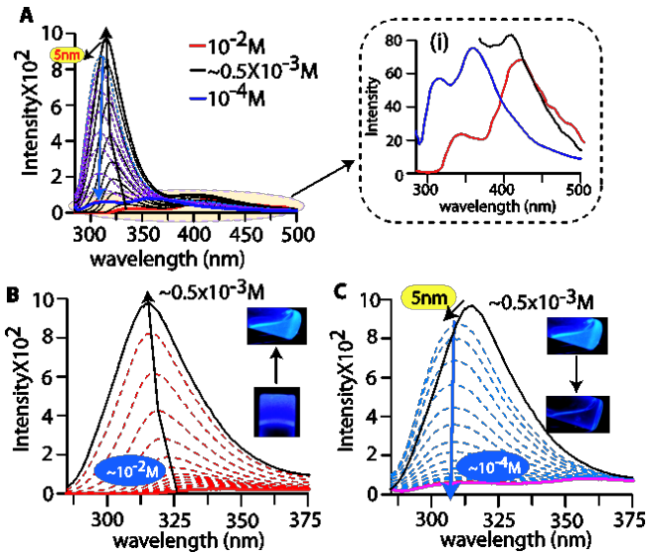

Figure 3.17 Dilution experiments followed by fluorecence spectroscopy (A) dilution of **CPH** from 10^{-2} (red line) to 10^{-4} (blue line) M, (i) is inset of A, (B) Dilution up to ~$0.5X10^{-3}$ M (black line) along with pictures of the gel and diluted gel under UV light and (C) Further dilution down to 10^{-4} M (blue line) and pictures of the corresponding vial under UV light.

The interactions involved in the aggregation and gelation process have been further investigated by ^{1}H NMR spectroscopy. The titration of $\mathbf{H_4T^{-L\text{-}tyr}}$ ($1.4x10^{-2}$ M, 400μL, deprotonated with 1.5 molar equivalents of LiOH) with Zn^{2+} ($2.8x10^{-2}$ M, 200μL) has been carried in D_2O (Figure 3.18). It needs to be mention that the deprotonation of $\mathbf{H_4T^{-L\text{-}tyr}}$ with LiOH is required to enhance the solubility of the pro-ligand in D_2O and to enable the formation of Zn^{2+} complexes. As expected, the spectrum of the deprotonated pro-ligand $\mathbf{H_4T^{-L\text{-}tyr}}$ shows seven signals resonating at δ_a=7.27 ppm (d, 4H, -Ph,), δ_b=6.95 ppm (d, 4H, -PhOH), δ_c=6.54 ppm (d, 4H, -Ph), δ_d=3.72 (d, 2H, $-CH_2Ph$), $\delta_{d'}$=3.54 (d, 2H, $-CH_2Ph$), δ_e=3.28 (t, 2H, −CHNH) and δ_f=2.75 (m, 4H, $-CH_2NH$) ppm. Adding aliquots of a stock solution of Zn^{2+} to the aforementioned sample was found to induce a significant broadening of all the signals accompanied by downfield shifts reaching maximum values ($\Delta\delta_c$ =0.15 ppm>$\Delta\delta_b$=0.07 ppm> $\Delta\delta_f$ ~$\Delta\delta_d$=0.05 ppm) after addition of 1 molar equivalent of metal, which is in agreement with the formation of 1:1 ($\mathbf{H_4T^{-L\text{-}tyr}}$:$Zn^{2+}$) coordination complexes. The largest downfield shift observed for the phenolic ring protons (H_c and H_b) is attributed to π−π interactions between phenolic rings presumably arranged in antiparallel stacks, a conclusion

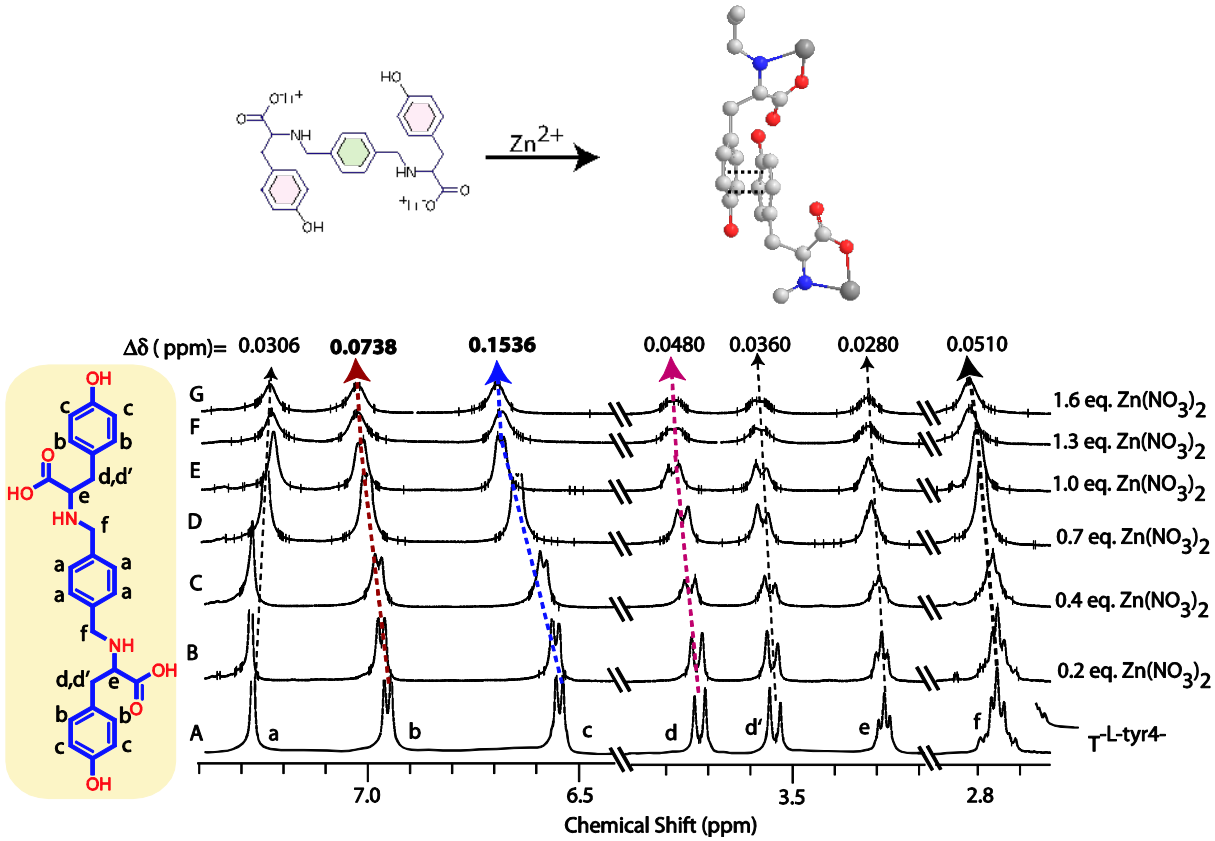

Figure 3.18 ^{1}H NMR titration of deprotonated $T^{-L\text{-}tyr4-}$ *vs.* $Zn(NO_3)_2$ in D_2O. $H_4T^{-L\text{-}tyr}$ structure along with labelling of proton (left side). The upper structure represents the result of ^{1}H NMR titration as well as possibility of π–π stacking between phenolic ring protons.

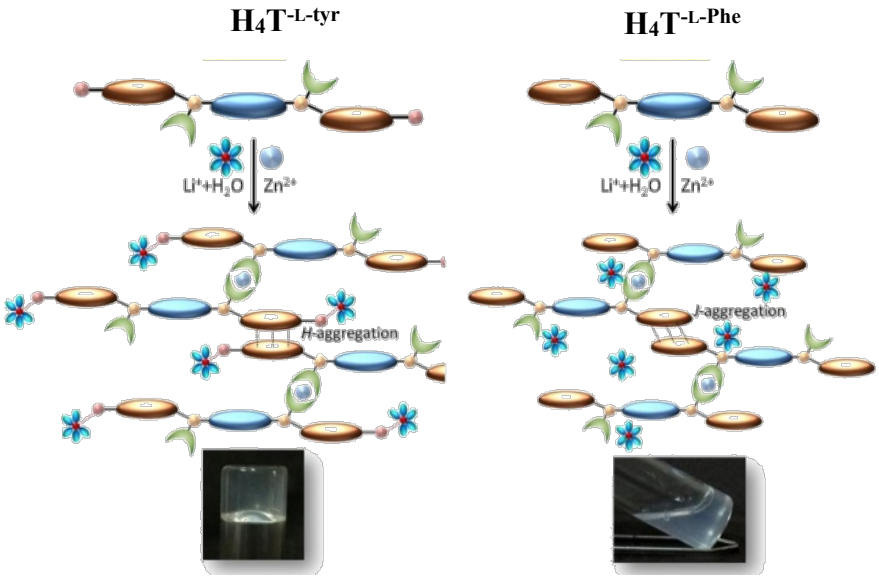

Figure 3.19 Model represents possibility of molecular arrangements for metallohydrogel and solution obtained from pro-ligands $\mathbf{H_4T^{-L\text{-}tyr}}$ and $\mathbf{H_4T^{-L\text{-}Phe}}$, respectively. (Gel formation fluorescence titration experiment (Figure 3.13B) suggests that after addition of $Zn(NO_3)_2$ to the deprotonated pro-ligand, molecules arrange them self into a higher energy state *via* blue

shift of 4 nm whereas deprotonated pro-ligand **H_4T^{-L-Phe}** shows red shift upon Zn^{2+} addition indicative towards the achievement of lower energy state *via J*-type aggregation.)

which is also supported by the PXRD and fluorescence data discussed above (Figure 3.18). By analogy, the small downfield shift $\Delta\delta_a$ = 0.0306 ppm observed for the protons of the central benzene ('I' in Figure 3.3) suggests a limited interaction of this aromatic ring with its closest neighbors.[46] At the same time, the downfield shift observed for the signals attributed to the aliphatic protons and to the 'I' benzene ring protons is due to a decrease of the electron density in **H_4T^{-L-tyr}** induced by its coordination to the Zn^{2+} ions.[48] The broadening of all the signals and the concomitant decrease of the signal-to-noise (S/N) ratio observed in the presence of Zn^{2+} is attributed to a significant increase in the viscosity on account of the gelation process.[49]

3.3.3 Complexation analysis

A comparative FT IR spectroscopic analysis of **H_4T^{-L-tyr}** and of the related xerogel was conducted to assess the role of each functional group in the gelation process. The FT IR spectrum of **H_4T^{-L-tyr}** displays intense vibration peaks centered at ν_{as}(COO)=1615 cm^{-1}, ν_b(–CH)=1455 cm^{-1}, ν_b(–OH, phenolic)=1331 cm^{-1} and ν_{str}(C–N)=1258 cm^{-1}. In the xerogel, these characteristic peaks appear shifted at ν_{as}(COO)=1631 cm^{-1} ($\Delta\nu$=16 cm^{-1}), ν(–CH)=1441 cm^{-1} ($\Delta\nu$=14cm^{-1}), ν_b(–OH, phenolic) absent and ν_{str}(C–N)=1247 cm^{-1} ($\Delta\nu$=11 cm^{-1}). Other key features include the absence of the bending vibration mode of the phenolic –OH, consistent with its deprotonation with LiOH, and the observation of a broad peak at ~3400 attributed to water molecules trapped within the gel matrix (Figure 3.20). The significant shift of most vibrations supports the existence of interactions between the >C=O, -NH and -OH moieties with the Li^+ and Zn^{2+} cations all along the gelation process.

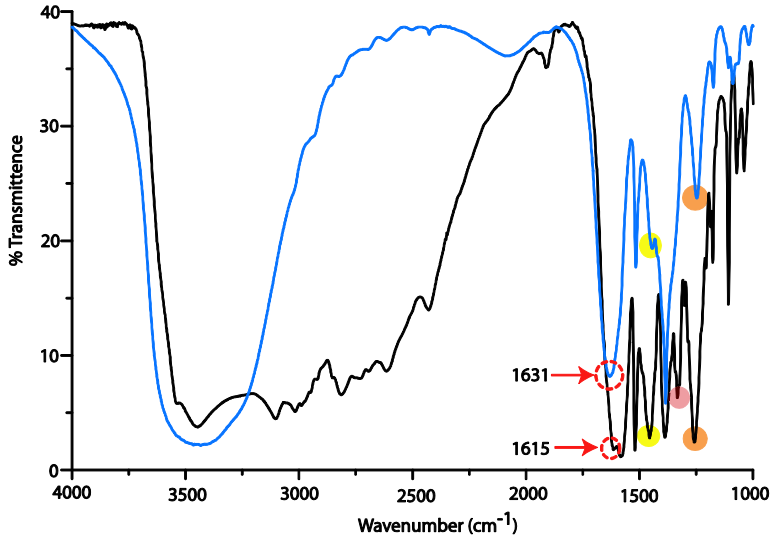

Figure 3.20 FTIR spectral overlap of $H_4T^{-L\text{-}tyr}$ (**$H_4T^{-L\text{-}tyr}$**, black line) and **CPH** (blue line).

Similar studies have been conducted with xerogels obtained from **CPH** and from **AuCPH,** mainly to gain insight into the interactions involved between [**$H_4T^{-L\text{-}tyr}$**/Zn^{2+}] and the AuNPs (Figure 3.21). The main difference observed between the FT IR spectra of both samples is the large shift of the diagnostic ν_{as}(COO) vibration, from 1631 cm^{-1} to 1615 cm^{-1}, associated to the formation of AuNPs. This clear experimental evidence support the conclusion that the carbonyl units are available over the surface of the nanofibers in the **CPH** gel and that they are involved in the directed growth of AuNPs (Figure 3.26).

The formation of coordination polymers and the stoichiometry of the association between **$H_4T^{-L\text{-}tyr}$** and Zn^{2+} have been scrutinized by absorption spectroscopy and by ESI-MS measurements. The method of continuous variation, also known as the Job's method, has been used to estimate the stoichiometry of the association.[50] Plotting the absorbance at 402 nm, which correlates with the concentration of complex formed in solution, as a function of the molar ratio x= $[Zn^{II}]/([Zn^{II}]+[T^{-L\text{-}tyr}]$ calculated at constant volume, led to the triangle shaped curve depicted in Figure 3.22B. The angular curvature of this plot featuring a max value at x=0.5 is fully consistent with a strong binding between **$H_4T^{-L\text{-}tyr}$** and Zn^{2+} in a 1:1

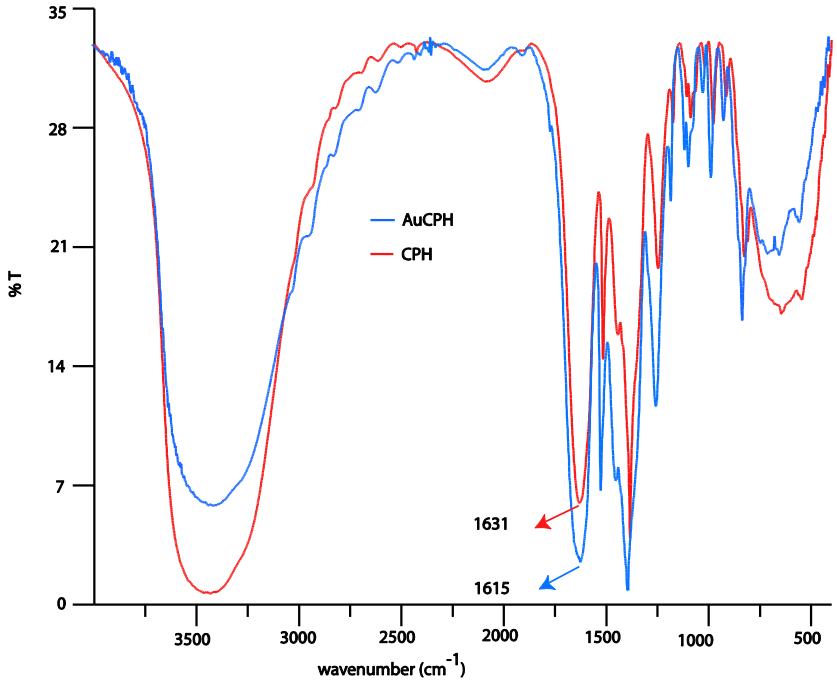

Figure 3.21 FTIR spectral overlap of **CPH** (red line) and **AuCPH** (blue line).

ratio (Figure 3.22). This stoichiometry was further confirmed by analysis of the ESI-MS spectrum of **CPH,** showing a peak at *m/z*= 527.1 attributed to the 1:1 coordination complex $[H_3T^{\text{-L-tyr}}+Zn]^+$ (calcd. *m/z*= 527.1), observed here as the repeating unit of the coordination polymer involved in metallohydrogel (Figure 3.22). The metal-driven self-assembly and the polymeric nature of the metallohydrogel is furthermore revealed through the observation of additional peaks at regular *m/z* intervals like at *m/z*= 615.1 ($[H_3T^{\text{-L-tyr}}/Li+Zn/NO_3/H_2O]^+$, *calcd*. *m/z*= 615.1), *m/z*= 675.0 ($[H_2T^{\text{-L-tyr}}/Zn_2+NO_3/H_2O]^+$, *calcd*. *m/z*= 675.2), *m/z* = 991.3 ($[(H_3T^{\text{-L-tyr}})_2/Zn/H]^+$, *calcd*. *m/z*= 991.3), *m/z* = 1063.2 ($[(H_2T^{\text{-L-tyr}})_2/Li/Zn_2]^+$, *calcd*. *m/z*= 1063.2) and *m/z* = 1119.1 ($[(H_2T^{\text{-L-tyr}})_2/Zn_3/H]^+$, *calcd*. *m/z*= 1119.3) (Figure 3.23). Thermogravimetric analysis of xerogel also suggests the presence of H_2O in strong association with gelator molecules (Figure 3.25). Taken together, the MS and Job's plot analysis support the conclusion that a 1:1 complexation between $\mathbf{H_4T^{\text{-L-tyr}}}$ and Zn^{2+} leads to the formation of long-range coordination polymers self-arranged into fiber-shaped

nanostructures involved in the gelation. The proligand **$H_4T^{-L\text{-}tyr}$** and its coordination with Zn^{2+} as well as the transformation of coordination polymeric molecules into long range fibers leading to gelation is well demonstrated though suitable model and chemical structures in figure 3.3 and 3.34, respectively, which are in well accordance with the experimental data obtained from various instrumental techniques such as FT IR, UV-vis, TEM, fluorescence, ESI-MS, Job's plot, TGA, ^{1}H NMR *etc.* and our previous work.[47]

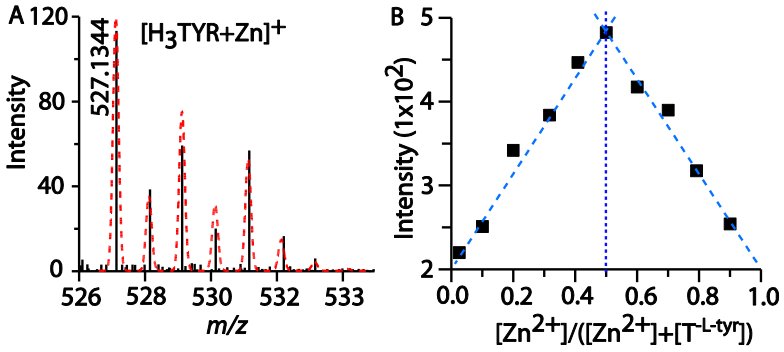

Figure 3.22 (A) ESI-MS spectra of asymmetric unit represents the experimental isotopic abundance pattern (black line) and simulated (red dotted line) and **(B)** Job's plot for LiOH deprotonated **$H_4T^{-L\text{-}tyr}$** *vs*. $Zn(NO_3)_2$.

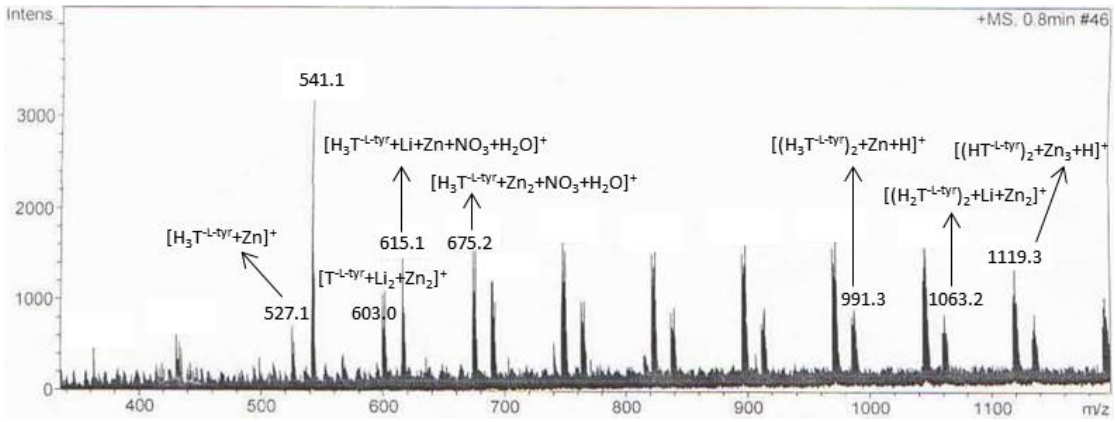

Figure 3.23 ESI-MS spectrum of diluted metallohydrogel (**CPH**) in positive mode along with labelling of molecular ion peaks.

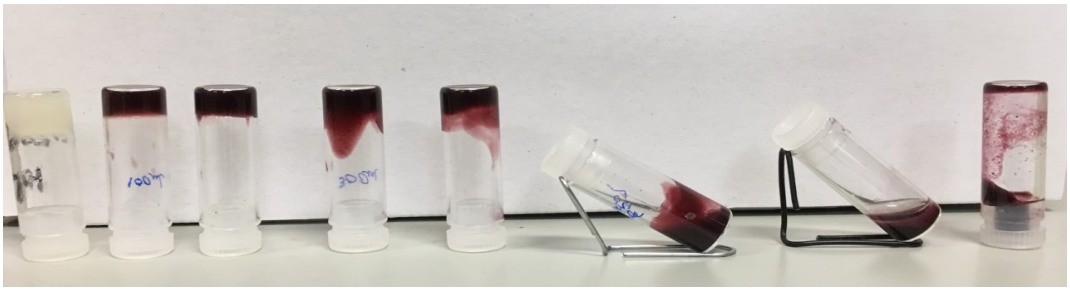

Figure 3.24 Effect of amount of $HAuCl_4$ solution addition to metallohydrogel weakens the gel strength.

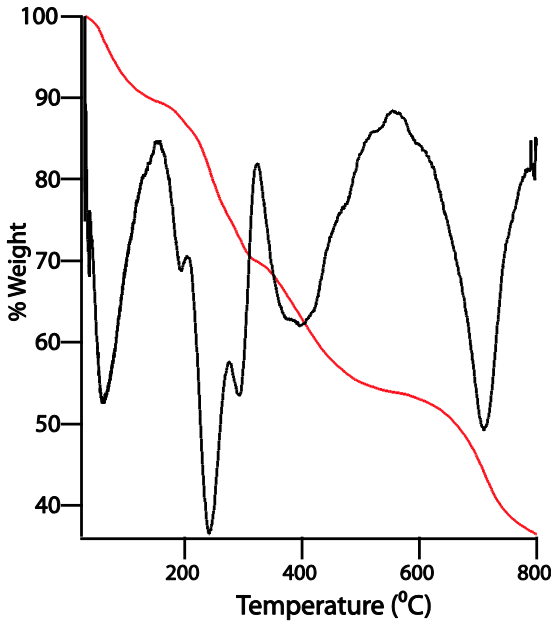

Figure 3.25 The Thermo Gravimetric Analysis (TGA, red line) along with derivative plot (black line) for the isolated compound from xerogel (washed with H_2O to remove extra salts and vacuum dried) shows weight loss of 10.46 % close to the molecular weight of $3H_2O$ (10.21 %). Three H_2O molecules were removed up to nearly ~180°C from xerogel which was indicative towards the presence of water in strong interaction with gelator molecule.

3.3.4 Nanofabrication and nanocatalysis

Metal-organic gel **CPH** samples have been used to achieve the synthesis of hybrid AuNPs-modified Nanofibers. The addition of a freshly prepared solution of $HAuCl_4$ (methanol/ether mixture) to the **CPH** gel sample kept under stirring led to an instantaneous color change from colorless to red brown, consistent with the formation of AuNPs inside the gel matrix (Figure 3.24). The latter AuNPs were submitted to in-depth characterizations using SPR (*ca.* 560 nm)

and TEM (*vide infra*). The latter studies revealed that using **CPH** gel as a medium enables a size-selective (~3 nm) and homogeneous growth of AuNPs throughout the sample, most probably due to the presence of suitable growth-directing functional groups uniformly distributed at the surface of the nanofibers (Figure 3.4). The size distribution is one of the most important parameter for applications in nanoparticle-based catalysis.[17,18,20]

The catalytic activity of the gel-embedded AuNPs has been evaluated towards the reduction of *p*-nitrophenol in the presence of $NaBH_4$. The progress and kinetics of the reaction have been followed/calculated from UV-vis absorption data recorded throughout the reaction. Addition of increasing amounts of $NaBH_4$ (15 mM in water) to *p*-nitrophenol (0.15 mM in water

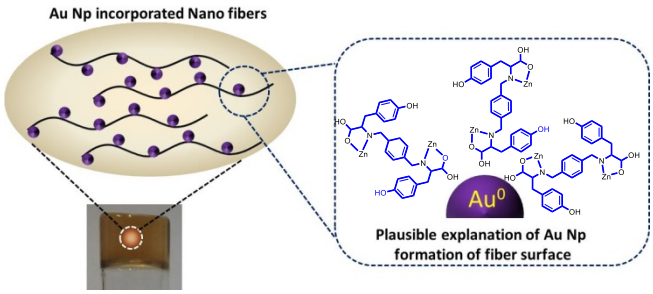

Figure 3.26 Schematic presentation of Au nanoparticles formation over nanofibers.

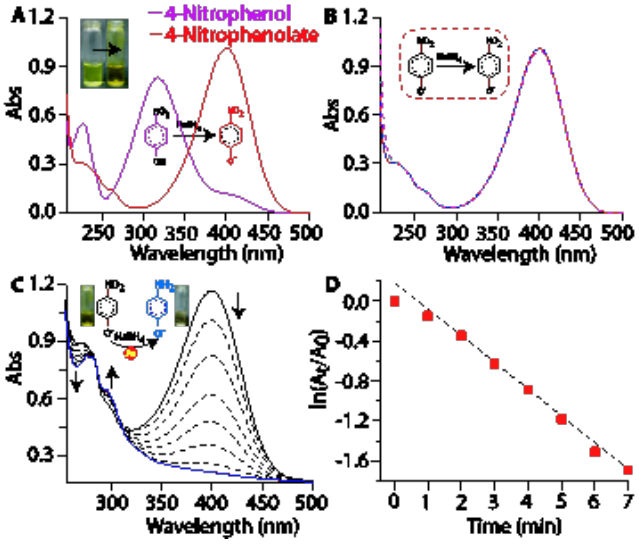

Figure 3.27 (A) *p*-nitrophenol (0.15 mM) before (violet line) and after (red line) addition of $NaBH_4$ (15 mM) solution; (B) 0.15 mM *p*-nitrophenolate with $NaBH_4$ (15 mM) without

AuNP as catalyst, (C) Reduction of *p*-nitrophenolate (0.15 mM) with $NaBH_4$ (15 mM) in the presence of AuNPs as catalyst originated from **AuCPH** at room temperature and (D) Plot of $\ln(A_t/A_o)$ *vs*. reaction time (min) showing pseudo-first order kinetics for metallogel.

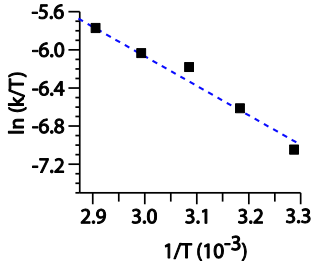

Figure 3.28 Eyring plot for reduction of *p*-nitrophenol to *p*-aminophenol using $NaBH_4$ in presence of catalyst AuNPs obtained from **AuCPH**.

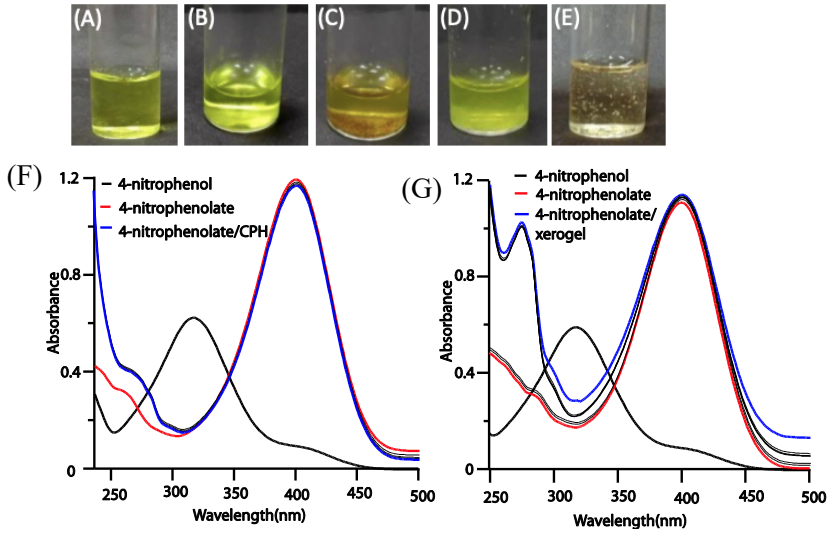

Figure 3.29 Pictures show (A) aqueous solution of 4-nitrophenol, the visual changes occurred upon addition of (B) $NaBH_4$ to aqueous solution of 4-nitrophenol, (C) xerogel (obtained from **AuCPH**) to 4-NP/$NaBH_4$ solution, (D) **CPH** to 4-NP/$NaBH_4$ solution, (E) **AuCPH** to 4-NP/$NaBH_4$ solution. UV-vis spectra of *aq.* 4-nitrophenol upon addition of (F) **CPH** and (G) dried **AuCPH** as catalytic material in presence of excess of $NaBH_4$ (100 equivalent of 4-nitrophenol).

H_2O) in the absence of AuNPs led to a significant modification of the absorption spectrum of the solution (going from light to intense yellow), including a loss of the initial signal at 318 nm at the expense of a new signal growing at 400 nm attributed to the accumulation of *p*-nitrophenolate ion (Figure 3.27).[51] Further addition of $NaBH_4$ up to 10 molar equivalents proved ineffective in promoting additional changes in the spectroscopic signature of the

sample even after 1 hour at room temperature, which confirms that a catalyst is needed to achieve the reduction of *p*-nitrophenol into *p*-aminophenol.

The same experiment carried out in the presence of catalytic amount of freshly prepared **AuCPH** (20 μL added to 2 mL reaction mixture) led to a fast decrease in the absorbance at λ_{max} =400 nm coming along with clean isosbestic points at 281 and 312 nm. It also led to the emergence of new peaks centered at 278 and 283 nm attributed to the conversion of *p*-nitrophenolate leading to the accumulation of *p*-aminophenol.[51] In our experimental conditions (2 mL of *p*-nitrophenol, 10 molar equivalents of $NaBH_4$, room temperature) a complete conversion was achieved in less than 7 minutes in the presence of a catalytic amount of **AuCPH**. In agreement with a pseudo first-order rate law, the kinetics of the reduction reaction was estimated from the linear plot of $\ln(A_t/A_0)$ *vs* time, where A_0 and A_t stand for the initial absorbance at t=0 and for the absorbance at t >0, respectively (Figure 3.27).[51] The apparent rate constant k_{app} corresponding to this pseudo first-order kinetics could be estimated at 305 K to 0.223 min^{-1} using Equation 3.1. From the data shown in figure 3.27 and 3.28 and equation 3.2 and 3.3, the E_a, $\Delta S^{\#}$ and $\Delta H^{\#}$ values corresponding to the **AuCPH**-catalyzed reduction of *p*-nitrophenol have then been estimated at 58.94 $KJmol^{-1}$, 244.09 $Jmol^{-1}K^{-1}$ and 4.41 $KJmol^{-1}$, respectively. These data fall in the range of energies reported in previous studies on nanoparticle-based reduction reactions.[52,53] The k_{app}, E_a, $\Delta S^{\#}$ and $\Delta H^{\#}$ values estimated for the same $NaBH_4$ mediated reduction reaction studied in the absence of **AuCPH** were found to be 0.014 min^{-1}, 595.14 $KJmol^{-1}$, -261.96 $Jmol^{-1}K^{-1}$ and 5.66 $KJmol^{-1}$, respectively. The similar reduction reaction was also carried out using dried **AuCPH** (xerogel) and **CPH** but both were unable reduce the 4-NP to 4-AP in presence of $NaBH_4$ and the rate constants found to be 0.019 min^{-1} and 0.018 min^{-1}, respectively, which is

very similar to only $NaBH_4$ mediated reduction reaction (Figure 3.29). This unique observation signifies the role of gel state in reduction reaction. Thus, comparative kinetics data collected with and without using **AuCPH** clearly demonstrate the beneficial role of **AuCPH** as catalyst in the reduction of *p*-nitrophenol reaction.

$$\ln\left(\frac{A_t}{A_0}\right) = -k_{app}t \qquad \textit{(Equation 3.1)}$$

$$\ln k_{app} = lnA - \frac{E_a}{RT} \qquad \textit{(Equation 3.2)}$$

$$\ln\left(\frac{k_{app}}{T}\right) = ln\left(\frac{k_B}{h}\right) + \frac{\Delta S^{\#}}{R} - \frac{\Delta H^{\#}}{R}\left(\frac{1}{T}\right) \qquad \textit{(Equation 3.3)}$$

Where E_a stands for the activation energy, A for the Arrhenius constant, R for the gas constant, T for temperature, h for the Planck constant, $\Delta S^{\#}$ for the activation entropy and $\Delta H^{\#}$ for the activation enthalpy.[52,53]

3.3.5 Rheological studies

The viscoelastic and mechanical properties of **CPH** as well as **AuCPH** have been investigated in comparative manner with dynamic oscillatory rheological measurements carried out on freshly prepared metallohydrogels (1% w/v) (Figure 3.30 and 3.31). The Stress sweep experiments (25 ^{0}C, 1Hz) show that the storage modulus (G′) is ~1 order of magnitude higher than the loss modulus (G″) for both the gels which proves the 'soft solid-like' nature of **CPH** as well as **AuCPH**.[54] The crossing for both the gels above 1 Pa is moreover consistent with a mechanical damage of the gel structure or with a phase transition. Further, the elasticity of **CPH** and **AuCPH** were measured as a function of the strain amplitude ranging from -0.5% to 2.0% at 10 rad s^{-1}. The storage modulus (G′) of about log 2.88 and log 2.4 measured at small strain (*f* -0.5%) reveals the initial stability of the gels toward the shearing process. At constant frequency (1Hz), the **CPH** was moreover found to be stable up

to ~1% strain with negligible effect over elasticity, while further strain leads to a deformation process followed by a phase transition from gel to sol, as revealed by the steep decrease in the values of both moduli and by the reversal of the viscoelastic signal (G″>G′).[55] On the other hand, **AuCPH** was found to be stable up to ~0.7% strain which also reveals that the **AuCPH** is slightly weaker strength gel than **CPH** (Figure 3.30 and 3.31).

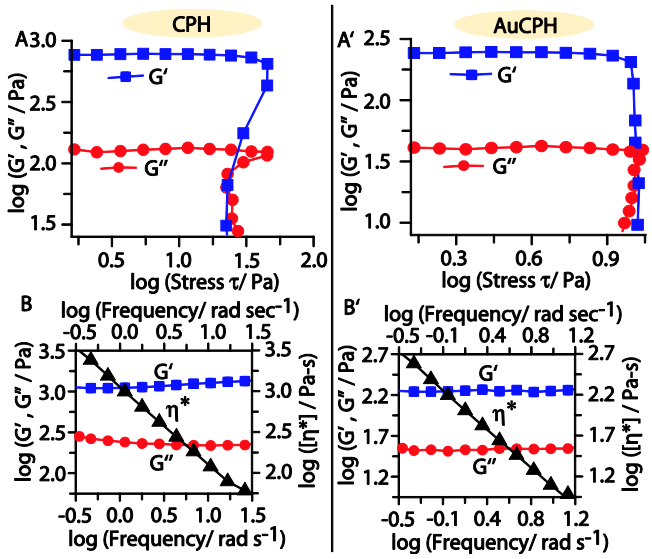

Figure 3.30 Rheology of **CPH** and **AuCPH** (A) and (A') Dynamic oscillation stress sweep of G′ (Loss modulus) and G″ (Storage modulus) *vs*. applied stress at frequency of 10 rad s^{-1} and temperature at 25 °C, (B) and (B') Primary axis: dynamic frequency sweep measurements of G′ and G″, at strain of 0.5%. Secondary axis: complex viscosity measurements.

Dynamic frequency sweep measurements carried out over **CPH** and **AuCPH** within the range -0.5- 1.5 rad s^{-1} and -0.5- 1.2 rad s^{-1}, respectively, which revealed a linear and constant variation of G′ and G″ with the applied frequency (ω), indicates that the gels are made of a stable network in both the metallogels (Figure 3.30 and 3.31).[56] In both the gels, the negative slopes (-1) of the logarithmic plot of the complex viscosity (η*) *vs* angular frequency (ω) also reveals constant declination of the viscosity with increasing frequency.[57] The curve shown in figure 3.31C also suggests that the viscoelasticity of the sample remains unchanged between 25-60 ^{0}C and that a deformation starts to appear above

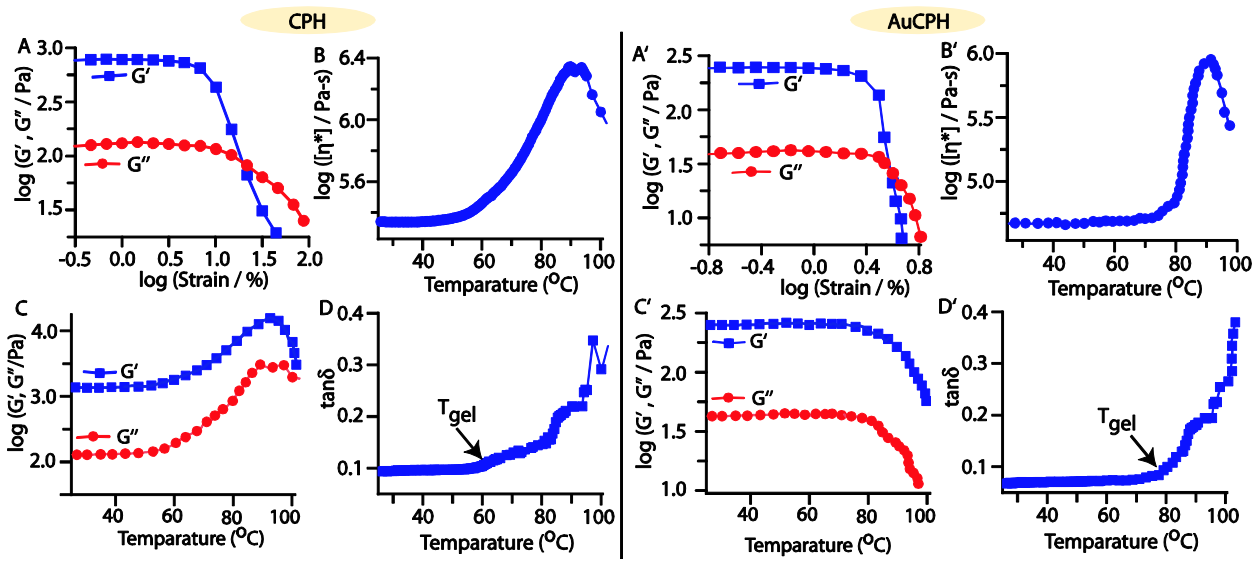

Figure 3.31 Rheology of **CPH** and **AuCPH** (A), (A') Dynamic strain sweep experiment at 10 rad s^{-1} and temperature 25 °C; (B), (B') Dynamic temperature ramp of complex viscosity measurement at 5 °C min^{-1}; (C), (C') Plot of G″ and G′ on dynamic temperature ramp and (D), (D') Dynamic temperature ramp of the loss tangent (tan δ = G″/G′) plot at 5 °C min^{-1}.

60 ^{0}C and reaches a maximum at 90 ^{0}C. The slow and long-range deformation observed between 60 and 90 ^{0}C, might be the reason behind the reversible gel-sol transition observed with **CPH** (Figure 3.6). The critical temperature corresponding the gel/sol phase transition in **CPH** (T_{gel}) was estimated at 93 ^{0}C from the graph shown in Figure 3.30D representing the loss tangent (tan δ= G″/G′) as a function of temperature.[58,59] The latter value and the thermal stability of the gel over a large temperature range was further confirmed with a plot of the complex viscosity versus temperature (Figure 3.30B). In contrast, **AuCPH** showed comparatively sharp gel transition temperature at ~80^{o}C which was further supported by a plot between complex viscosity and temperature (Figure 3.31).

3.3.6 Conductance studies

The conductance properties of freshly prepared **CPH** samples have been investigated by impedance measurements. The primary objective was to gain insight into the conductivity of

the samples but also to follow the ageing phenomena, and to determine the influence of temperature and of the alkali ions on the electrical properties of the gels. The conductivity responses recorded over time with different LiOH, NaOH or KOH-based gel samples were found to follow the same trend, with a relatively fast decrease of the conductance in the first stage of the measurement (0-3h), leading to a loss of about 2-3% of the initial value, followed by an apparent stabilization on a longer time scale (t >4h). Carrying out these time-dependent measurements on a larger time scale still revealed a further drift of the conductivity values losing another 1-3 % over one week. To summarize, the conductivity of **CPH** as initiator have been found to be quite stable over time (t_0: 507.6 mS.m^{-1} → t_0 +7 days: 489.9 mS.m^{-1}). The reproducibility of the impedance responses has been checked with different samples synthesized following the same experimental procedure. The latter could be significantly improved upon developing a systematic synthetic procedure involving use of a

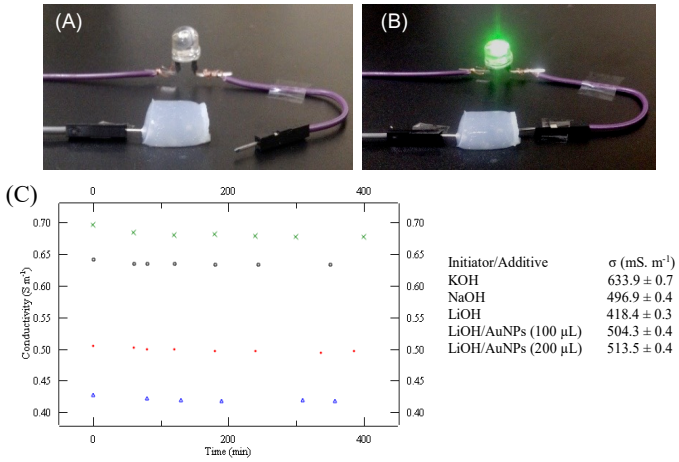

Figure 3.32 (A) and (B) Metallohydrogel (1% w/v) is used as a bridge to complete an electrical circuit where a green LED bulb was lit with a DC voltage. (C) (Left) Cation dependence of the conductivity measured over time (0-400 min) on gel (Li^+, Na^+ and K^+) or liquid (Cs^+) samples at 295K (green cross: CsOH, black square: KOH, red circle: NaOH, blue triangle: LiOH). (Right) Conductivity values (mS m^{-1}) measured at 295K and t = 240 min on four different gels produced from KOH, NaOH, LiOH, and LiOH + a given volume (V_{AuNP}) of a freshly prepared $HAuCl_4$ solution ($HAuCl_4$, 10^{-1} mol L^{-1} in methanol/diethylether).

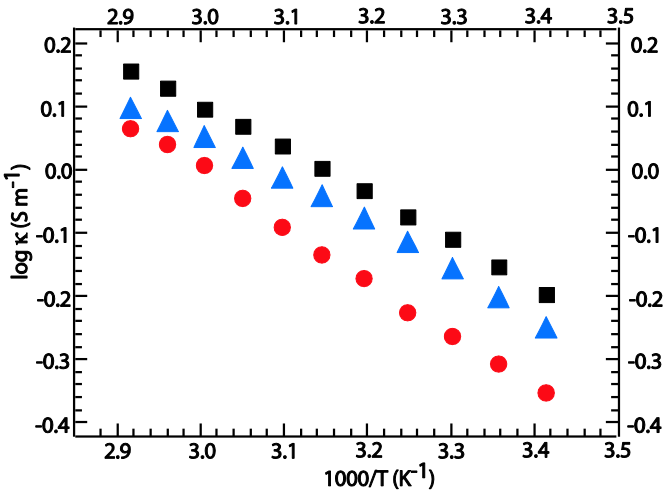

Figure 3.33 Temperature dependence (298-343 K) of the ionic conductivity measured on different gels samples (blue triangle: LiOH, red circle: NaOH, black square: KOH).

programmable syringe pump enabling an accurate control over the addition rate of the Zn^{2+} solution. Most importantly, we found the electrical properties of the gels to be strongly dependent on the alkali metal ions used as initiators.[3,43-46,57,58] This effect is clearly brought to light in figure 10 with data recorded for samples prepared with the same procedure involving either LiOH, NaOH, KOH or CsOH as key reactants. One of the conclusions drawn from these data is that the significant drop in the conductivity values observed along the series $Cs^+>K^+>Na^+>Li^+$ is rather driven by the bulk properties of the gels than by the conductivity of their components. Based on simple visual observations, it was indeed established that the most rigid gels could systematically be obtained with LiOH while CsOH only led to hardly viscous solutions. The values plotted in figure 10 thus reveal the gelating ability of the different alkali ions used as initiators and not their intrinsic ionic conductivity (related to their mobility and decreasing in the following order $Li^+>Na^+>K^+>Cs^+$). The most rigid gels obtained with Li^+ are thus less conductive on account of the restricted mobility of the charge carriers, while the most liquid samples obtained with Cs^+ give rise to much higher conductivity was found to increase with temperature in a similar

manner for all the investigated samples. The linear evolution of the log κ= f(1/T) curves between 298K (1000/T = 3.3) and 323 K (1000/T = 3.1) (Figure 3.33) also support the conclusion that the gels samples are fully stable in this temperature range. The noticeable change in the slope of the log κ= f(1/T) curves observed beyond 343 K is then compatible with a significant modification of the gel sample induced upon heating. This conclusion is consistent with the rheology data discussed in the previous section, revealing that an increase in temperature leads to a hardening of the gel.

Similar impedance measurements have been carried out on **CPH** samples doped with Au nanoparticles (**AuCPH**) (Section 3.2 and Figure 3.24). The amount added (V_{AuNP}) was found to have a great influence on the properties and firmness of the resulting samples, going from well behaved gels (obtained for small V_{AuNP} values) to viscous or fully liquid solutions (obtained for large V_{AuNP} values).

The amount added (V_{AuNP}) was found to have a great influence on the properties and firmness of the resulting samples, going from well behaved gels (obtained for small V_{AuNP} values) to viscous or fully liquid solutions (obtained for large V_{AuNP} values) as demonstrated in Figure 3.24. Suitable gel samples could be obtained repeatedly in these conditions for loadings (V_{Au}) falling in the range 100-200 µL. Suitable gel samples could be obtained repeatedly in these conditions for loadings (V_{Au}) falling in the range 100-200 µL. Impedance measurements carried out on these samples revealed that the addition of V_{AuNP} leads to a significant increase of the conductivity, *i.e.* from ~418 $ms.m^{-1}$ measured in the absence of AuNPs to ~513 $ms.m^{-1}$ measured on the gel sample prepared after addition of 200 µL of the $HAuCl_4$ solution. Here again, the improvement in conductivity could be attributed to changes in the steadiness of the gels rather than to the conductivity of the AuNPs.

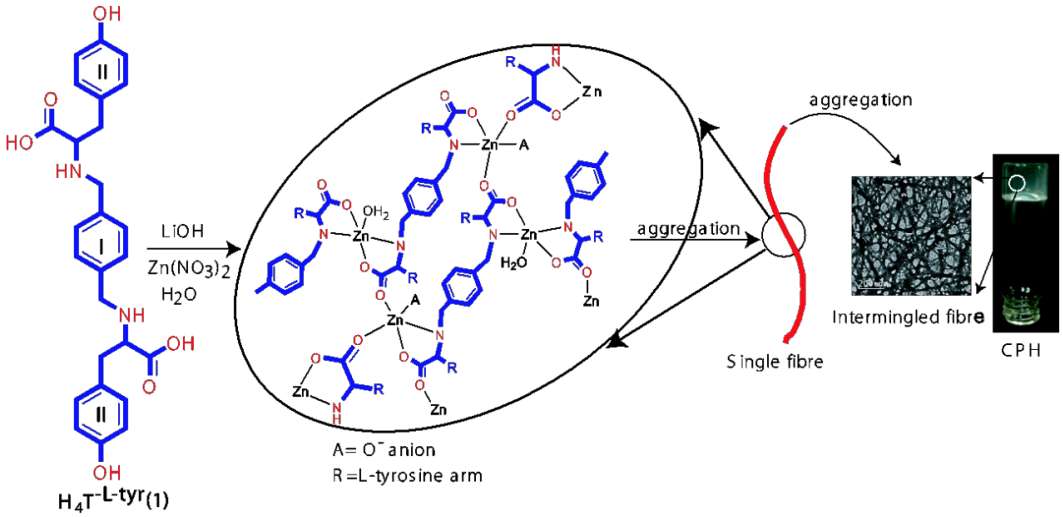

Figure 3.34 A schematic presentation of plausible mechanism behind metallohydrogel formation.

3.4 Conclusion

In conclusion, through this chapter, we have described a fluorescent metallohydrogel (**CPH**) involving a coordination polymer as a key building element. The mechanism of gelation has been investigated using FTIR, NMR, fluorescence, impedance, TEM, PXRD and rheological measurements. The selective combination of $\mathbf{H_4T^{-L\text{-}tyr}}$/$Li^+$/$Zn^{2+}$ was not only found to result in the fluorescence of the metallohydrogel, but it also proved responsible for the formation of conducting nanometric fiber-shaped assemblies. These nanofibers have been used as growth platforms to achieve the fabrication of uniform sized AuNPs (*ca.* 3-4 nm) in the absence of any external reducing agent. The AuNP-doped nanofibers (**AuCPH**) have proved useful as catalytic material in the reduction of *p*-nitrophenol with $NaBH_4$. For the first time, in the case of metallogel, we calculated complete kinetics data for the abovementioned model reduction reaction. The conductance properties of these metallohydrogels (**CPH** and **AuCPH**) have also been explored and shown to be strongly dependent on the size of the alkali ions and on the temperature. We believe that this concept of metallogel will open up new perspectives for the development and applications of soft materials in the field of electronics and catalysis.